

Design loads for wave impacts – introducing the *Probabilistic Adaptive Screening* (PAS) method for predicting extreme non-linear loads on maritime structures

Sanne M. van Essen^{a,b,*}, Harleigh C. Seyffert^a

^aDepartment of Maritime & Transport Technology, Delft University of Technology (TU Delft), Delft, The Netherlands

^bShips Department, Maritime Research Institute Netherlands (MARIN), Wageningen, The Netherlands

ARTICLE INFO

Keywords:

Extreme value prediction
Design loads
Wave impacts
Ships
Offshore structures
Coastal structures
Non-linear loads
Probabilistic design
Reliability
Green water
Slamming

ABSTRACT

Wave impact loads on a maritime structure can cause casualties, damage, pollution of the sea and operational delays. Their extreme (or design) values should therefore be considered in the design of these structures. However, this is challenging because these events are both rare and complex, requiring high-fidelity computation and long analysis durations to obtain such design loads. Existing extreme value prediction methods are not tailored or validated for wave impacts. We therefore introduce the new *Probabilistic Adaptive Screening* (PAS) method for predicting extreme non-linear loads on maritime structures. The method introduces a probabilistic approach to multi-fidelity screening, allowing efficient linear potential flow indicators to be used in the low-fidelity stage, even for strongly non-linear load cases. The method is validated against a range of cases, including non-linear waves, ship vertical bending moments, green water impact loads, and slamming loads. It can be concluded that PAS accurately estimates both the short-term distributions and extreme values in these test cases, with most probable maximum (MPM) values within 10% of the available full brute-force Monte-Carlo Simulation (MCS) results. In addition, PAS achieves this performance very efficiently, requiring less than 4% of the high-fidelity simulation time needed for conventional MCS. These results demonstrate that PAS can reliably reproduce the statistics of both weakly and strongly non-linear extreme load problems, while significantly reducing the associated computational cost. The present study validates the statistical PAS framework; further work should focus on validating the full procedure including CFD load simulations, and on validating it for long-term extremes.

1. Introduction and background

1.1. Wave impacts

A *wave impact* on a ship, offshore, or coastal structure is a dynamic loading event that occurs when a water wave hits the structure, causing a rapid transfer of momentum. It may occur when such a maritime structure encounters large and steep waves, experiences large wave-induced motions, or some combination of both (see Figure 1). The resulting loads can cause significant damage, endanger crew or inhabitants, cause pollution of the sea by lost cargo, decrease performance of the structure, or (in rare occasions) endanger the structure itself. Examples include green water and slamming on ships, wave-in-deck loads on offshore structures, and impacts on wind turbines, breakwaters, dams, jetties, bridges, and other coastal infrastructure. Severe wave impact accidents are documented on sailing ships [1–4] and offshore structures [5–9]. Wave impacts also affect the structural reliability of various coastal structures, ranging from breakwaters [10, 11], offshore wind turbines [12], bridges [13], port infrastructure [14], lighthouses [15], to residential buildings [16, 17]. This makes accurate prediction of the distributions and extreme values of strongly non-linear loads, such as those due to wave impacts, essential. Waves and wave-induced processes are stochastic, so designing for them requires *probabilistic design methods*. The aim of such methods is not to avoid all accidents, but to ensure that the probability of failure of the considered structure remains below an acceptable level.

1.2. Requirements for accurate prediction of extreme wave impact loads

As also discussed in [18], obtaining extreme (or design) values for wave impact loads is very challenging because such events are both rare and complex. Converged statistics of rare events can only be obtained from long-duration

*Corresponding author


 s.m.vanessen@tudelft.nl / s.v.essen@marin.nl (S.M. van Essen); h.c.seyffert@tudelft.nl (H.C. Seyffert)
ORCID(s): 0000-0001-8239-0724 (S.M. van Essen); 0000-0003-0323-2096 (H.C. Seyffert)



Figure 1: Two examples of wave impacts on marine structures: a wind turbine foundation near Fécamp in 2023 (left, photo: K. King) and research vessel *Discoverer* on the Bering Sea in 1979 (right, photo: R. Behn / NOAA).

x' / x'' \hat{x}	LF / HF version of variable x MPM of variable x	RWE VBM	Relative Wave Elevation Vertical Bending Moment	n_{it} N P_{exp} R_{19p} T_{exp} $T_p / T_{p,e}$ V_s V_{hog} / V_{sag} z ϵ_1 / ϵ_2 μ ω / ω_e	# wave encounters in MCS # seeds in MCS PoE level corr. to T_{exp} and $T_{p,e}$ RWE at station 19 (from potential flow) Target / exposure duration Peak wave (encounter) period Forward speed of the ship Hogging / sagging VBM # bootstrapping copula draws Case-specific stopping criteria limits Wave heading w.r.t. structure Wave (encounter) frequency
AS	Adaptive Screening method	C	Wave crest height		
CFD	Computational Fluid Dynamics	$C(u, v)$	Fitted copula model		
EVPM	Extreme Value Prediction Method	$[d^*, h^*]$	Predicted HF distrib.		
HF	High-Fidelity	$[d_{H,b}^{cop}, h_b^{cop}]$	Distrib. HF copula draw b		
LF	Low-Fidelity	$[d_{L,b}^{mcs}, l_{mcs}]$	Distrib. all LF samples in MCS		
MCS	Monte-Carlo Simulation	$[d_{L,b}^{sel}, l_{sel}]$	Distrib. present LF samples		
MD	Acquisition function	F_x	Green water force		
MVPD	Acquisition function	F_{pd1}	Bow-flare slamming force		
MPM	Most Probable Maximum	h^{sel}	Present HF samples		
PAS	Probabilistic Adaptive Screening	m	# present HF samples		
PoE	Probability of Exceedance	n	# LF indicator peaks in MCS		

Box 1: Most important nomenclature, where distrib. = distribution.

analysis, whereas we need high-fidelity (HF) simulations to resolve complex physics. HF models in this context can be Computational Fluid Dynamics (CFD) or basin experiments. The ability of CFD to reproduce wave impact loads in a given wave event improved rapidly in recent years (see e.g., [19]), but simulating durations in the order of the lifetime of a maritime structure is not yet feasible in practical design contexts. Using a dedicated extreme value prediction method (EVPM) can reduce the HF simulation duration, and such an EVPM for strongly non-linear loads should:

1. Be a multi-fidelity method, integrating elements of HF models for accurate loads, and LF models to handle rare event statistics;
2. Account for the practical limitation that only a few wave events can be simulated with a HF model during the design stage;
3. Allow for some wave non-linearity in the LF model, since linear models neglect important factors such as wave breaking and higher-order interactions that drive wave impact complexity;
4. Preserve consistent LF and HF time profiles, because peak loads are not always most relevant for structural dynamics (rise times or impulses can be more critical);
5. Have a flexible framework that allows case-specific LF and HF models while preserving the overall methodology, enhancing general applicability;
6. Provide accurate extreme values for strongly non-linear loads, validated using real-world cases;
7. Be efficient and practical for use in design.

1.3. Existing methods and their shortcomings

A literature review of maritime EVPMs can be found in [20], and [18] added recent literature on both EVPMs and related reliability methods. Summarising, some existing methods satisfy multiple EVPM criteria, but their implementations remain case-specific and untested for strongly wave impact loads. Given these gaps, industry practice for extreme wave impact loads follows standards (e.g., [21–28]), specifying plate thicknesses, or alternative direct analysis methods using experiments with multiple 0.5 to 3 h wave seeds for short-term extreme response estimates.

To address the limitations of existing methods relative to the requirements in Section 1.2, we previously developed the Adaptive Screening (AS) method [18]. AS is a multi-fidelity approach for predicting extreme non-linear HF wave-induced loads on maritime structures. It uses an LF variable as an indicator to select critical wave events, which are then evaluated with an HF tool to obtain non-linear loads. The framework constructs a surrogate HF distribution from these events, from which probabilistic design loads are derived. The procedure is iterative, adding new HF samples until convergence. AS was validated through a weakly non-linear case (second-order waves) and a moderately non-linear case (vertical bending moments), and further assessed in a third pilot study on a strongly non-linear case (green water impact loads on a containership)¹. Further work [29] studied the effect of the *acquisition function*, one of the elements of AS. Most data and all scripts are available in [30, 31]. The strength of AS for strongly non-linear loads lies in its flexibility (it allows for a wide range of LF indicator variables, including non-linear ones) and in its efficiency (it is optimised to minimise the number of HF simulations). These make the method well-suited for problems with significant non-linearity and sparse datasets. This was supported by [18], which demonstrated good performance for a range of non-linear cases. However, the method also has limitations for complex problems. Selecting an appropriate indicator may require a relatively expensive ‘LF’ model, such as the coarse-mesh CFD used in Case 3 of [18]. This produced accurate results, but the LF MCS became costly. While AS remains far more efficient than a full HF MCS, this additional cost can reduce its practicality in early design stages when computational resources are limited. A poorly chosen indicator may also lead to a non-conservative bias in the estimated design loads. This can be mitigated with a safety factor, but this is not ideal. Thus, AS meets all requirements in Section 1.2 for simple cases, but it cannot always be efficient and accurate simultaneously in complex cases (it either fails on accuracy or on efficiency).

The existing methods (including AS) generally do not account for the full dependence structure and joint extremes of the LF and HF variables. This may be the reason for some of their shortcomings, for instance the bias introduced by AS when it is applied to complex cases. Copula models offer a flexible way to describe such dependencies. A copula model is a statistical framework for multivariate distributions that decouples marginal behavior from dependence. Compared to directly fitting a joint distribution, copulas can more effectively capture tail dependence, even with limited samples. Copula modelling of joint dependencies was e.g., recently used in reliability analysis of slopes in spatially variable soils based on limited sample data [32, 33], in reliability analysis of systems consisting of dependent equipment parts [34, 35], in reliability-based design optimisation for correlated variables [36, 37] and to study the joint risk of different relevant variables for the overtopping of breakwaters [38]. In extreme value analysis, copulas were used in similar ways to model the joint tail distribution of different variables (e.g., [39]) and to model the dependence of loads in a mooring line and sea state parameters [40]. Copula models have been used by oceanographers to model the joint statistics of dependent environmental variables (e.g., [41–44]) or to handle spatial dependency between extreme environmental variables (e.g., [45–47]). Considering wave impact loading, copula models have also been used to model the joint distribution of the quasi-static and impulsive contributions of experimentally measured vertical wave impact pressures on a deck box [48], wave impact maxima on a coastal bridge conditioned on a minimum wave impact rise time [49], extreme wave-induced stresses simultaneously measured at two different deck locations of a container vessel [50], the interaction of different parameters of an experimental dam break wave impact event [51], the joint probability of the maxima and rise times of wave impact loads on breakwaters [52], and to derive the most likely wave impact load profile on a floating wind turbine as a function of the wave parameters [53]. Copula models have also been combined with multi-fidelity modelling before: [54, 55] defined multi-fidelity forms of importance sampling, and [56] used multi-fidelity modelling for reliability problems combined with a copula model to establish the model hierarchy. Earlier studies also combined copula modelling with adaptive sampling: [57, 58] combined Bayesian model updating with Monte Carlo Simulation (MCS) and copulas in reliability analysis, and [59] used a Bayesian model with a copula to capture the joint annual extremes of climate variables that change over time.

Despite their promise, copula-based approaches have, to our knowledge, not yet been combined with multi-fidelity or adaptive sampling frameworks to improve the efficiency of extreme value prediction (or reliability analysis) for wave impact loading (or other strongly non-linear loads). The work done by [54, 55] is closest to this, but these studies rely on importance sampling rather than adaptive sampling and have not been tested on real-world strongly non-linear cases similar to the wave impact problem. Adaptive sampling is generally considered more flexible and robust than importance sampling for complex tail behaviour.

¹In the AS papers, we used *non-linear responses* to emphasise the method’s applicability to hydrodynamic motions, accelerations, green water loads etc. However, as discussed in Section 1.3, extreme value prediction aligns with reliability analysis, where *loads* is the standard term. We therefore now use *loads* for all hydrodynamic responses.

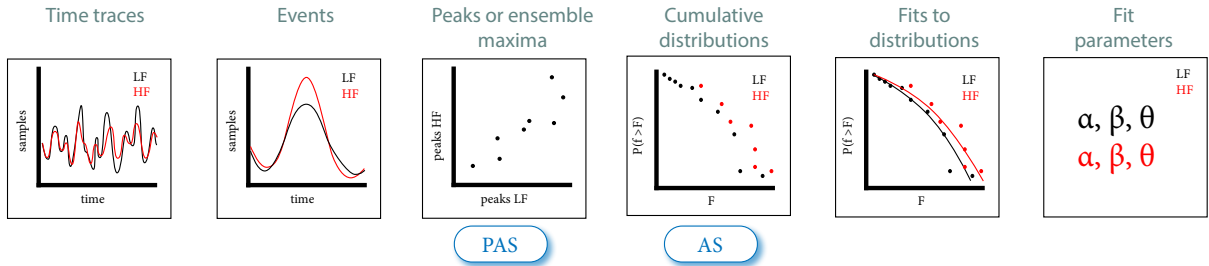


Figure 2: Some of the possible *statistical levels* where multi-fidelity methods can derive or learn the relation between a LF indicator variables (black) and HF non-linear loads (red), including the location of AS and PAS. Modified from [18].

1.4. Paper objectives & contribution

As discussed above and in [18], we need a new EVPM for wave impact loads. Serious incidents with maritime structures still occur at sea, and existing EVPMs are not suitable and / or validated for this problem. Therefore we propose a modification to AS that addresses its limitations in complex, strongly non-linear cases. AS relies on LF order statistics as surrogates for HF order statistics, making performance highly sensitive to the choice of LF indicators (often requiring relatively expensive ‘LF’ models). Our new approach keeps the efficient screening and adaptive sampling components, but replaces the order-statistics assumption with a copula model linking LF indicators and HF loads. This enables us to derive the full HF distribution from a limited HF sample, reducing sensitivity to indicator choice, decreasing bias, and ensuring any remaining bias is conservative (unlike the non-conservative AS approach). Consequently, the modification reduces dependence on relatively expensive LF models (e.g., allowing the use of indicators from linear potential flow instead of from coarse mesh CFD), while improving both accuracy and applicability in design contexts. This especially benefits strongly non-linear problems, where suitable LF indicators for AS are computationally costly to obtain. The related objectives of this paper are to:

1. Introduce a modification of AS, called *Probabilistic Adaptive Screening* (PAS), which improves the prediction of extreme values of strongly non-linear loads, and complies with the requirements in Section 1.2.
2. Validate that the method can (more) accurately and efficiently predict short-term extreme values (than AS) for a range of realistic strongly non-linear applications.
3. Show that this can also be done in combination with indicators derived from linear potential flow calculations instead of from coarse mesh CFD.

The novelty of PAS lies not in the individual method elements, but in the integration of screening, adaptive sampling, and copula fitting to multi-fidelity data. Combining screening and adaptive sampling provides efficiency, while copula fitting ensures that joint extremes between LF indicators and strongly non-linear HF wave-induced loads are properly captured. In theory, PAS can predict both long-term (over a ship’s lifetime in various wave conditions or *sea states*) and short-term (within single sea states) extreme values. However, in this work we validate it for short-term extremes, since only HF short-term wave-impact data are available (and even those were difficult to obtain). Still, this provides a clear demonstration of the method’s capabilities. Summarising, this work contributes a new, efficient, and accurate EVPM specifically tailored to wave impact loads and validated for that purpose.

1.5. Layout

Section 2 presents the new PAS method, and Section 3 introduces four case studies that are used to validate PAS, and to compare it to AS. These include two applications from [18] (second-order waves and vertical bending moments), and add two new strongly non-linear wave impact cases (green water impact forces and bow-flare slamming forces on a sailing ship). Subsequently, Section 4 explains the metrics we used to validate the method’s performance, after which Section 5 presents and discusses the results. Finally, Section 6 draws conclusions.

2. The Probabilistic Adaptive Screening (PAS) method

Multi-fidelity methods connect LF indicators and an HF loads at different *statistical levels* (see Figure 2). To the left of this figure: retaining more information leads to greater accuracy but requires complex solution strategies and more HF samples. To the right: simplifying the system reduces HF samples but risks losing critical information. [18]

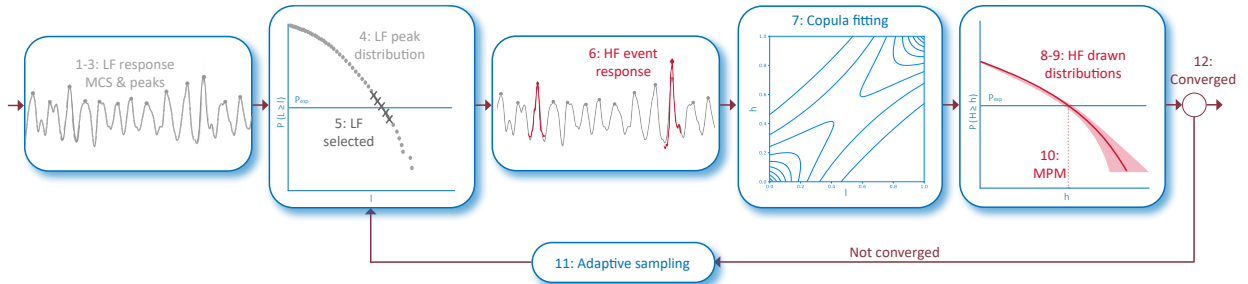


Figure 3: Schematic illustration of PAS, where the numbers roughly correspond to the method steps in Section 2.1. The left plot only shows a small part of the MCS time traces, and only a few HF samples are included in the middle and right distributions to illustrate the principle.

explained that AS was developed at the cumulative distribution level, but in complex cases this approach may have discarded too much information. It may be easier and more robust to model the joint distribution of paired LF-HF peak values than to model differences between their marginal cumulative distributions. In practice, a single LF value may correspond to multiple HF outcomes. This variability is naturally represented in the joint distribution framework but not in the AS method, which implicitly assumes a one-to-one mapping between LF and HF values. In the *Probabilistic Adaptive Screening* (PAS) method, we therefore apply our model for the LF-HF relationship at the level of the LF and HF peaks instead. We use a copula model to do this, and include the copula basics in Appendix B: general theory, formulations of the copulas used in the PAS method, a description of the parameters in each of these copula, and the relation of these parameters to the dependence structure of the fitted data.

2.1. Steps

A schematic overview of PAS is provided in Figure 3, and the method involves the steps described below. The numbers in the figure roughly correspond to these steps. Each step is labelled to indicate whether it is inherited from the AS method or new.

- Step 1 LF indicator, unchanged:** Define a LF indicator with a strong statistical relation to the target HF response, as would be done in a screening method or AS. The indicator signal is not necessarily the same signal at a different fidelity level as the target HF response; it can also be another signal with similar order statistics as the target HF response. An ideal LF indicator has identical order statistics as the target HF non-linear response, where the highest LF indicator value appears in the same wave event as the highest HF non-linear response value, and so on. See [20] for a review of suitable wave impact indicators. The similarity requirements between the LF indicator order statistics and the HF load order statistics are less stringent in PAS than in AS. This simplifies indicator selection and, by permitting lower-fidelity indicators, accelerates Step 2.
- Step 2 LF Monte-Carlo simulation, unchanged:** Perform LF Monte-Carlo Simulations (MCS) for a large number N of wave seeds, each with the same exposure duration T_{exp} . This exposure duration is the duration for which you want to obtain the extreme value of the response in a single sea state. This is generally the duration for which the hydrodynamic response is expected to remain ergodic (roughly 15 min to 3 h, depending on wave ergodicity, speed and course changes, etc.). The total MCS should be significantly longer than T_{exp} to obtain converged extreme values. See [60, 61] for an example of the required N for wave crests, green water impact forces, and wave-in-deck impact forces. The total MCS duration T_{tot} follows from $T_{\text{tot}} = NT_{\text{exp}}$.
- Step 3 LF peaks, unchanged:** Identify all n LF indicator peaks in the full MCS duration T_{tot} . This can be done in different ways; here we use peak-over-threshold crossings. Also find the number of zero up-crossing encountered wave crests n_w within T_{tot} , which can be estimated from Equation (1) if there is no explicit wave record available. Here $T_{p,e}$ is the peak wave encounter period, which is different from the peak wave period T_p if the (ship) response has forward speed. They are related using the absolute wave frequency $\omega = 2\pi/T$ and Equation (2), where ω_e is the wave encounter frequency, V_s is the forward speed of the ship and μ is the wave heading with respect to the ship (π is head waves in the sign convention). n_w is the basis for all distributions presented from here on, which enables us to use LF indicators and HF responses with a different number of peaks.

$$n_w \approx NT_{\text{exp}}/T_{p,e} \quad (1)$$

$$\omega_e = \omega - \omega^2 V_s \cos \mu / g \quad \rightarrow \quad T_{p,e} = T_p / (1 - (2\pi V_s \cos \mu) / (T_p g)) \quad (2)$$

Step 4 **LF distribution, unchanged:** Calculate the LF probability of exceedance (PoE) for all indicator peaks $\mathbf{d}_L^{\text{mcs}} = \{d_{L,i}^{\text{mcs}} | i = 1, 2, \dots, n\}$, related to the number of wave encounters, by applying Equation (3). The largest LF indicator peak value has a PoE of $1/n_w$ and the smallest n/n_w . We now have a LF indicator peak PoE distribution dataset $[\mathbf{d}_L^{\text{mcs}}, \mathbf{l}^{\text{mcs}}]$, where \mathbf{l}^{mcs} contains all indicator peak values, in descending order corresponding to the ascending PoE values in $\mathbf{d}_L^{\text{mcs}}$.

$$\mathbf{d}_L^{\text{mcs}} = P(\mathbf{l}^{\text{mcs}} \geq l) \cdot \frac{n}{n_w} \quad (3)$$

Step 5 **Initial LF samples, unchanged:** Select initial samples from the LF MCS dataset of the previous step. The selected set is called $[\mathbf{d}_L^{\text{sel}}, \mathbf{l}^{\text{sel}}]$, where $\mathbf{d}_L^{\text{sel}} = \{d_{L,k}^{\text{mcs}} | k = 1, 2, \dots, m\}$ and $\mathbf{l}^{\text{sel}} = \{l_k^{\text{mcs}} | k = 1, 2, \dots, m\}$. Different sampling strategies can be used to determine these indices k . Here we select these events around the PoE corresponding to T_{exp} based on the LF MCS dataset: the *probability of interest*. This P_{exp} is given in Equation (4). We pick m PoE values that span a range around P_{exp} and call them $[p_1, p_2, \dots, p_m]$. Now we use Equation (5) to add the elements in $\mathbf{d}_L^{\text{mcs}}$ closest to these values to the selected set, and the corresponding elements from \mathbf{l}^{mcs} . The resulting selected set $[\mathbf{d}_L^{\text{sel}}, \mathbf{l}^{\text{sel}}]$ is a subset of the full available LF MCS set $[\mathbf{d}_L^{\text{mcs}}, \mathbf{l}^{\text{mcs}}]$. Note that selecting samples around P_{exp} is also used in alternative RCM's such as those by [62, 63].

$$P_{\text{exp}} = N/n_w \approx T_{p,e}/T_{\text{exp}} \quad (4)$$

$$d_{L,k}^{\text{mcs}} = \left[\arg \min_{d \in \mathbf{d}_L^{\text{mcs}}} |p_k - d| \right] \text{ for } k = 1, 2, \dots, m \quad (5)$$

Step 6 **Corresponding HF samples, unchanged:** Find the corresponding HF response for the wave events corresponding to $[\mathbf{d}_L^{\text{sel}}, \mathbf{l}^{\text{sel}}]$, by running CFD calculations or experiments for these selected events. This new dataset of HF samples is called $\mathbf{h}^{\text{sel}} = \{h_k | k = 1, 2, \dots, m\}$, here h_k is the HF non-linear response value maximum for event k .

Step 7 **Copula fitting, new:** Fit a bivariate copula to the LF-HF data $[\mathbf{l}^{\text{sel}}, \mathbf{h}^{\text{sel}}]$. Let $F_{\mathbf{l}^{\text{sel}}}$ and $F_{\mathbf{h}^{\text{sel}}}$ denote the fitted marginal distributions of the LF and HF samples, respectively, obtained here as kernel-smoothed cumulative distribution functions. These marginals are used to transform the original data into pseudo-observations \mathbf{u} and \mathbf{v} on the unit interval $[0, 1]$ (see Equation (6), where $\text{rank}()$ denotes the statistical rank of the LF or HF elements). This is a necessary step since copula models are defined on $[0, 1]^2$. A dynamic copula selection procedure (see Section 2.2) is then applied to choose, at each iteration, the best-fitting copula $C(u, v)$ for the paired data $[\mathbf{u}, \mathbf{v}]$ from among the bivariate Gaussian, Clayton, Gumbel, and Frank copula models. The fitting workflow is illustrated in Figure 4. The selected copula model may vary between iterations.

$$\begin{aligned} u_i &= \frac{1}{m+1} \text{rank}(l_i^{\text{sel}}) \approx F_{\mathbf{l}^{\text{sel}}}(l_i^{\text{sel}}) \\ v_i &= \frac{1}{m+1} \text{rank}(h_i^{\text{sel}}) \approx F_{\mathbf{h}^{\text{sel}}}(h_i^{\text{sel}}), \quad i = 1, \dots, m \end{aligned} \quad (6)$$

Step 8 **Draw HF samples, new:** Draw a set of HF values from the fitted copula model, conditioned on the full set of LF values in the MCS \mathbf{l}^{mcs} from Step 4 (with elements $l_j^{\text{mcs}} | j = 1, \dots, n_w$). This sampling is performed 20 times in a bootstrapping procedure to reduce sampling uncertainty ($z=20$). First, we construct \mathbf{u}^{mcs} , the pseudo-observations obtained by evaluating the fitted LF marginal distribution at the LF values in \mathbf{l}^{mcs} (see Equation (7)). For each bootstrap realisation $b = 1, 2, \dots, z$ and each conditioning point j , we draw a random variable $r_{(j,b)}$ from the uniform distribution (Equation (8)), where ϵ is a small constant introduced to prevent numerical instabilities. We then compute the conditional copula quantile (i.e., the inverse conditional CDF) using Equation (9), where

$C(u, v)$ is the best-fitting copula selected in the previous step. Finally, the bootstrap realisations of the predicted HF datasets, $\mathbf{h}_b^{\text{cop}}$, are obtained using Equation (10).

$$u_j^{\text{mcs}} \approx F_{\text{sel}}(l_j^{\text{mcs}}), \quad j = 1, \dots, n_w \quad (7)$$

$$r_{j,b} \sim U(\varepsilon, 1 - \varepsilon), \text{ where: } \varepsilon = 10^{-6} \quad (8)$$

$$v_{j,b}^{\text{cop}} = C_{V|U}^{-1}(r_{j,b} | u_j^{\text{mcs}}) \quad (9)$$

$$h_{j,b}^{\text{cop}} = F_{\text{h}^{\text{sel}}}^{-1}(v_{j,b}^{\text{cop}}) \quad (10)$$

Step 9 HF distribution, new: Calculate the HF PoE distribution of the HF copula-drawn samples of Step 8 for each bootstrapping realisation, using Equation (3) applied to $\mathbf{h}_b^{\text{cop}}$. Similar as for the LF distribution in Step 4, the largest HF sample drawn from the copula has a PoE of $1/n_w$ and the smallest n/n_w (the number of HF copula-drawn samples is equal to n). For each draw in the bootstrapping process we now have a HF PoE distribution dataset $[\mathbf{d}_{H,b}^{\text{cop}}, \mathbf{h}_b^{\text{cop}}]$. Then we compute the mean distribution and its U95% sampling uncertainty over these bootstrapping realisations. The result of this procedure is a mean estimated HF distribution $[\mathbf{d}^*, \mathbf{h}^*]$, and its sampling uncertainty in the present iteration.

Step 10 Estimate MPM, unchanged: Estimate the target short-term extreme value from $[\mathbf{d}^*, \mathbf{h}^*]$ of Step 9. As explained in Section 1.4, our primary target is the HF MPM value \hat{H} , found using Equation (11). The sampling uncertainty of the MPM can be derived from the bootstrapped copula draws in the same way. This is illustrated by the horizontal line in the right subfigure of Figure 3.

$$\mathbf{d}^*(\hat{H}) = P_{\text{exp}}, \quad \text{therefore: } \hat{H} = \mathbf{d}^{*-1}(P_{\text{exp}}) \quad (11)$$

Step 11 Adaptive sampling, unchanged: Start the adaptive sampling procedure, iterating over Step 5 to Step 11. In each iteration, an acquisition function is applied to define a new sample, unless convergence is reached. The new samples are selected from $[\mathbf{d}_L^{\text{mcs}}, \mathbf{l}_L^{\text{mcs}}]$ defined in Step 4, without replacement. The required formulations are discussed in Section 2.4 (acquisition function) and Section 2.5 (stopping criterion). When a new HF sample is defined as discussed there, it is added to the LF selected set $[\mathbf{d}_L^{\text{sel}}, \mathbf{l}_L^{\text{sel}}]$ in Step 5, after which Step 6 to Step 11 are repeated.

Step 12 Convergence, unchanged: When convergence is reached according to the criterion, the result is the converged prediction for the HF distribution \mathbf{h}^* over prediction range \mathbf{d}^* , the associated MPM value \hat{H} , and the MPM uncertainty.

A key advantage of both AS and PAS is the integration of adaptive sampling with screening, which enables efficient generation of new HF samples at targeted low PoE values and avoids the need for extensive HF simulations, which is not possible with adaptive sampling alone. This feature makes the methods especially effective for extremes of strongly non-linear responses. The additional advantage of PAS over AS is that the copula fitting provides a stronger statistical foundation and makes the method less sensitive to the choice of indicator. This enables the use of linear potential flow indicators to predict design loads for wave impacts, which is very computationally efficient.

The steps of PAS are presented in general terms, making the method flexible and adaptable to any strongly non-linear problem with suitable LF and HF analysis tools. To apply this general method, several choices must be made: the indicator variable and its calculation tool in Step 1, the MCS length in Step 2, the event definition method in Step 3, the selection of initial critical events in Step 5, the HF tool and initialisation of this tool based on the LF wave event in Step 6, the type of copula and fitting method in Step 7, the number of bootstrapping realisations of the copula-generated samples in Step 8, the target extreme value in Step 10, and the acquisition function, number of samples per iteration, and stopping criterion in Step 11. Sections 2.3 to 2.5 provide suitable choices for the wave impact problem.

The MPM predicted in Step 10 corresponds to the $q = e^{-1} \approx 0.368$ quantile of the short-term distribution for linear Gaussian processes (following the Rayleigh distribution, see e.g., [64]). This means that the probability that

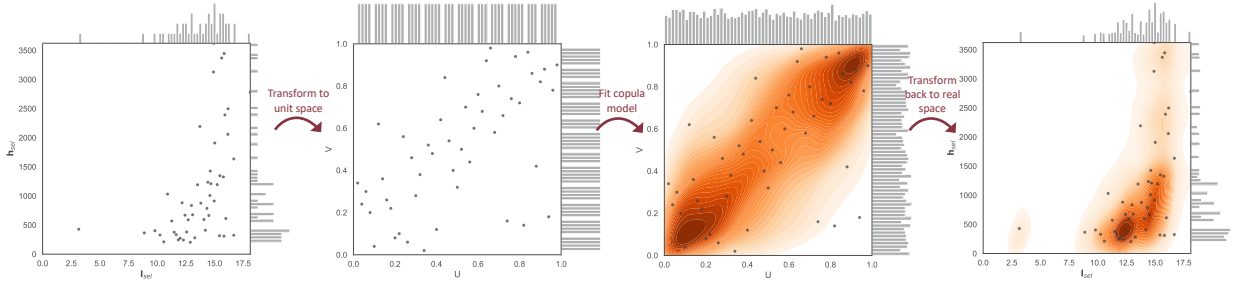


Figure 4: Example copula-fitting procedure (here shown for case 3a of the present paper at 40 iterations), with from left to right: scatter diagram of the LF-HF data, the corresponding pseudo-observations in uniform U,V-space, the fitted copula model in U,V-space, and the transformed data from the copula model in the ‘real’ data space.

the maximum response over the target exposure duration exceeds the MPM is 62.3%. The offshore industry often prefers higher quantiles for design. We can estimate these by replacing P_{exp} in Equation (11) with $P_q = 1 - q^{m/n}$ [23]. However, this necessitates an even longer LF MCS to achieve converged results. More research is needed to evaluate the applicability of the method for higher quantiles.

A challenging aspect of all screening-based methods, including (P)AS, is the initialisation of HF event simulations in Step 6. This requires reproducing LF wave events in CFD or experiments and raises the question of how to define HF input conditions for a (statistically) equivalent LF event. Several possible solutions are discussed in Section 5.

2.2. Copula selection

In Step 7, we do not know in advance which copula best fits the paired LF-HF dataset. This may also change per iteration. As we want to limit the number of HF samples as much as possible, we cannot rely on formal bootstrap-based goodness-of-fit tests such as Cramér–von Mises or Kolmogorov–Smirnov (these have low power on small datasets). The goal of our selection is not to prove that one copula is the true one, but to pick at a given iteration the most plausible copula model. We compared four candidates (bivariate Gaussian, Gumbel, Clayton, and Frank, see Appendix B.2). Both the Gaussian and Frank copulas are used for symmetric, linear-type dependence without tail emphasis, but Frank has more uniform spread in the data than Gaussian. Clayton is used for strong lower tail dependence and Gumbel for strong upper tail dependence. First, each copula was fitted to the paired pseudo-observations $[\mathbf{u}, \mathbf{v}]$ from Equation (6). We estimate the parameters of the candidate copulas using the method of moments (MoM) based on Kendall’s τ . This is formulated in Equation (12), where $\theta(\tau)$ denotes the copula family’s analytic relation between Kendall’s τ and its parameter (see Appendix B.2). Next, we use the maximised log-likelihood $\ell(\hat{\theta})$ in Equation (13) to select the best-fitting copula out of the four candidates, where C is the copula density evaluated at the pseudo-observations $[\mathbf{u}, \mathbf{v}]$, and $\hat{\theta}$ is the estimated copula parameter. The copula with the largest $\ell(\hat{\theta})$ is selected in each iteration.

$$\hat{\theta} = \theta(\hat{\tau}), \quad \hat{\tau} = \frac{2}{m(m-1)} \sum_{1 \leq i < j \leq m} \text{sign}((u_i - u_j)(v_i - v_j)) \quad (12)$$

$$\ell(\hat{\theta}) = \sum_{i=1}^m \log C(u_i, v_i; \hat{\theta}) \quad (13)$$

2.3. Initial sampling

The outcome of Bayesian or adaptive / sequential sampling methods (such as PAS) can depend on the initial sampling, because the initial data shape the first prediction, which in turn influences subsequent updates. If the initial samples do not sufficiently represent the true variability of the system, the prediction may converge more slowly or toward a biased region. To avoid this, we selected a relatively large initial sampling pool of 9 LF samples in Step 5 (so also 9 initial corresponding HF samples in Step 6). These LF samples were selected as follows: the 4 largest LF indicator values in the MCS, plus 5 samples that were selected using uniformly spaced indices over the remaining part of $\ln(\mathbf{d}_L^{\text{mcs}})$ from Step 4.

2.4. Adaptive sampling and acquisition function

To limit the number of costly HF calculations for strongly non-linear loads, the acquisition function in Step 11 is used. We use a function that selects one new HF sample per iteration. In [29], AS was evaluated using seven acquisition functions. Functions that distribute samples uniformly along the logarithmic PoE axis or that concentrate around P_{exp} , were found to be effective. These insights are also useful for PAS. However, the HF distribution in PAS is constructed differently, making several of those functions unsuitable. Copula fitting requires HF samples over a wider range than just around P_{exp} . For this reason, PAS uses the maximum-distance *MD* acquisition function, which selects new samples based on their largest separation from existing HF points on the logarithmic PoE axis. This aligns with the construction of the initial sample pool described above.

For each iteration i in Step 5, we define $p_{\text{new},i}$ as the optimal PoE for adding a new LF sample to the existing set of selected samples $\mathbf{d}_L^{\text{sel}}$. We drop the iteration index i for convenience. The HF samples available in the current iteration are then written as $[\mathbf{d}_H^{\text{sel}}, \mathbf{h}^{\text{sel}}]$, with $\mathbf{d}_H^{\text{sel}} = \{d_1^s, d_2^s, \dots, d_m^s\}$ ordered such that $d_1^s < d_2^s < \dots < d_m^s$. The MD function is then formulated in Equation (14). The new point is located halfway between $\ln(d_k^s)$ and $\ln(d_{k+1}^s)$, where the gap $[\ln(d_{k+1}^s) - \ln(d_k^s)]$ is the largest among all pairs of consecutive selected samples. The function operates on the logarithm of PoE to focus on the tail of the distribution.

$$p_{\text{new}}^{\text{md}} = \arg \max_{k \in \{1, \dots, m-1\}} \left(\frac{\ln(d_{k+1}^s) - \ln(d_k^s)}{2} + \ln(d_k^s) \right) \quad (14)$$

This would be the best new sample value to add to $\mathbf{d}_{L,i}^{\text{sel}}$ in Step 5 (including iteration subscript i again). However, in PAS, we only have the LF samples in the available LF MCS sample pool of Step 4. We therefore always select the sample from $\mathbf{d}_L^{\text{mcs}}$ closest to $p_{\text{new},i}^{\text{md}}$, without replacement (see Equation (15), where $d \in \mathbf{d}_L^{\text{mcs}} \setminus \mathbf{d}_{L,i}^{\text{sel}}$ indicates that d is chosen from the set $\mathbf{d}_L^{\text{mcs}}$ excluding the elements in $\mathbf{d}_{L,i}^{\text{sel}}$). The new sample $d_{L,i}$ is added to the existing LF pool $[\mathbf{d}_{L,i}^{\text{sel}}, \mathbf{l}_i^{\text{sel}}]$ in Step 5 for the next iteration.

$$d_{L,i} = \arg \min_{d \in \mathbf{d}_L^{\text{mcs}} \setminus \mathbf{d}_{L,i}^{\text{sel}}} \left| \ln(p_{\text{new},i}^{\text{md}}) - \ln(d) \right| \quad (15)$$

2.5. Stopping criterion

We stop the procedure when new iterations no longer produce significant changes in the predicted PoE distributions. A similar stopping criterion was used in [18] for AS, but some changes were made to match it to PAS. For PAS, we use a stopping criterion consisting of two parts. The first part sets a limit for the mean absolute difference between each set of subsequently predicted distributions. The second part was based on the coefficient of variation (COV) of the MPM value over a number of the last iterations. The complete formulations for this stopping criterion are detailed in Appendix C. This appendix also explains how this criterion is different from the criterion used for AS in [18].

2.6. Assumptions

The most important assumption in PAS is the similarity between the order statistics of the LF indicator and the HF response in Step 9. Most alternative methods, such as response-conditioning methods and other screening techniques discussed in [20], also rely on this assumption. Its validity depends on the indicator choice; a poorly chosen indicator can significantly reduce the result accuracy. However, introducing the copula fitting technique in PAS reduces the weight of this assumption, as it makes the LF-HF coupling probabilistic instead of deterministic. This reduces the impact of outliers in the order statistics comparison. Another critical assumption in Step 6 is that the HF tool accurately calculates the true HF event response. Previous studies have shown that CFD can effectively predict wave impact loads if wave kinematics and ship motions are modelled well (see e.g., [19, 65, 66]). Additionally, [67] demonstrated that screening results could serve as effective inputs for such calculations. Finally, PAS assumes that the LF-HF mapping of each problem fits one of the candidate copula models (bivariate Gaussian, Clayton, Gumbel or Frank). The dynamic best-fitting selection procedure in Step 7 already reduces the method's reliance on a single copula model. The present study shows that this assumption works for a wide range of considered test problems.

2.7. Implementation

The PAS framework, including iterative procedure, acquisition functions and stopping functions were implemented in custom Python scripts. We used the Python *copulas* package (v0.12.0) to define and fit the Archimedean copulas

Table 1

Summary of considered cases, where AC = accommodation, BF = bow flare, BW = breakwater, GW = green water, PF = potential flow, RWE = relative wave elevation at station 19 of the ferry, VBM = vertical bending moment, T_{MCS} = MCS duration, T_{exp} is defined in Step 2 of PAS, n_w in Step 3 and P_{exp} in Step 5. Cases 1a,b and 2a are identical to those evaluated with AS in [18].

Case	Structure	HF variable	HF source	LF indicator	LF source	Cond. Table 2	T_{exp} [h]	T_{MCS} [h]	n_w [-]	P_{exp} [-]
1a	-	2 nd -order waves	Analytical	Lin. waves	Analytical	A	1:00	50:00	16364	3.06×10^{-3}
1b	-	2 nd -order waves	Analytical	Lin. noisy waves	Analytical	A	1:00	50:00	16364	3.06×10^{-3}
2a	Ferry	Hogging VBM	Non-linear PF	Hogging VBM	Linear PF	B	0:30	30:00	14359	4.18×10^{-3}
2b	Ferry	Sagging VBM	Non-linear PF	Sagging VBM	Linear PF	B	0:30	30:00	14359	4.18×10^{-3}
3a	Ferry	GW force AC	Experiments	RWE	Linear PF	C	0:30	34:49	15198	4.58×10^{-3}
3b	Ferry	GW force AC	Experiments	RWE	Linear PF	D	0:30	23:43	10900	4.35×10^{-3}
4a	Ferry	Slam force BF	Experiments	RWE	Linear PF	C	0:30	34:49	15198	4.58×10^{-3}
4b	Ferry	Slam force BF	Experiments	RWE	Linear PF	D	0:30	23:43	10900	4.35×10^{-3}

Table 2

Summary of irregular wave conditions (all with a JONSWAP spectrum) and operational conditions used in the cases, where H_s is significant wave height, T_p is peak wave period, $s = 2\pi H_s / (g T_p^2)$ is the non-dimensional wave steepness, γ is the peak enhancement factor of the JONSWAP spectrum, h is water depth, μ is the ship-fixed wave direction (180 deg is head waves), V_x is the forward speed of the ship or structure, V_y is its transverse drift speed, and $T_{p,e}$ is the corresponding peak wave encounter period.

Name	H_s [m]	T_p [s]	s [-]	γ [-]	h [m]	μ [deg]	V_x [m/s]	V_y [m/s]	$T_{p,e}$ [s]	Comment
A	10.0	11.0	0.053	3.3	30.0	-	-	-	-	No ship
B	13.2	10.0	0.085	3.0	1000.0	180	5.1	0.0	7.5	
C	8.1	9.4	0.059	3.3	179.9	150	2.4	0.4	8.2	
D	8.3	10.0	0.053	3.3	179.9	150	5.0	0.6	7.8	

(Gumbel, Clayton, Frank). For the bivariate Gaussian copula we defined a custom class. All scripts are available in the 4TU repository: [68].

3. Cases

As explained in the introduction, we applied PAS (and AS for reference) to four cases, each with a variation. Table 1 provides an overview of these cases, where the corresponding wave and ship operating conditions are listed in Table 2. These particulars are explained in more detail in the corresponding sections below. For all cases, we used the settings in Section 2 for PAS, and we used 2 initial samples and MF-GPR for AS. The *ground truth* MPM values from the validation dataset for all cases are included in Table 3 (the rest of this table is explained later).

3.1. Case 1 (weakly non-linear): second-order wave crest heights

Case 1 from [18, 29], with related datasets in [30, 31], addresses a weakly non-linear problem. We predict extreme values of ‘HF’ second-order wave crest heights C'' , in long-crested steep waves (condition A in Table 2). The HF validation dataset consisted of analytical second-order wave time traces according to [69]. Two LF indicators were defined: linear Gaussian wave crests C'_{good} (case 1a) and crests in the same linear Gaussian waves including an additional noise wave system C'_{worse} (case 1b). The LF MCS of Step 2 was done for 50 hours duration. Since the HF variable is analytically tractable, it was easy to generate long HF ground truth time traces for this example case. Appendix D shows a scatter plot of LF indicator versus HF validation response peaks. This plot shows that the LF and HF order statistics align closely, but not perfectly. Linear wave crests are a good indicator for second-order wave crests, so this is logical. To generate a new HF sample in each iteration, we used the matched LF and HF peaks. When an event was selected based on its LF indicator value (in Step 5 or Step 11), the corresponding HF value was drawn from the matched LF-HF peaks. This is only possible because we have an analytically traceable HF variable; in reality, each iteration would require a new HF event calculation. We aim to predict the HF one-hour MPM value \hat{C}'' . Summarising:

- HF target extreme value: one-hour MPM second-order wave crest height \hat{C}'' .
- LF indicator: linear waves C'_{good} (1a), linear noisy waves C'_{worse} (1b).

To monitor convergence, we set stopping criteria limits for $S(j)$ in Equation (27): $\epsilon_1 = 0.1$ m for the maximum absolute wave crest distribution difference (around 0.7% of the maximum HF value in the validation dataset), and $\epsilon_2 = 0.05$ for the coefficient of variation of the one-hour MPM value (standard deviation 5% of mean). These limits are more lenient than those used for AS in [18]. To ensure a fair comparison, we applied these to both AS and PAS.

3.2. Case 2 (moderately non-linear): vertical bending moments

Case 2 from [18, 29], with related datasets in [30, 31], studies a moderately non-linear problem. We predict extreme values of hogging vertical bending moments (VBM) on a 190 m ferry in extreme irregular head waves (condition B in Table 2). The HF VBM in hogging mode V''_{hog} and sagging mode V''_{sag} were generated using a non-linear (Froude-Krylov) potential flow simulation, while the LF VBM in hogging mode V'_{hog} and sagging mode V'_{sag} were generated using a linear potential flow simulation. The hogging peaks were defined by the zero up-crossing troughs in these VBM simulations; the sagging peaks by the zero up-crossing peaks. Unlike in case 1, this HF response is not analytically tractable, but 30-hour HF MCS non-linear simulations to produce validation material were feasible. The LF-HF peak scatter plots are shown in Appendix D. This shows that, as expected, the LF and HF VBM peaks have less similar order statistics than those of the first- and second-order wave crests in case 1. For further details on the case, see [18] (which only included the hogging peaks). We aim to predict the HF 30-minute MPM values $\widehat{V''_{\text{hog}}}$ and $\widehat{V''_{\text{sag}}}$. As this case concerns a sailing ship it would be unrealistic to assume constant wave conditions, heading, and speed for longer than a 30-minute duration. Summarising:

- HF target extreme value: 30-minute MPM weakly non-linear hogging $\widehat{V''_{\text{hog}}}$ (2a) and sagging $\widehat{V''_{\text{sag}}}$ (2b) VBM.
- LF indicator: linear hogging V'_{hog} (2a) and sagging V'_{sag} (2b) VBM.

To monitor convergence (see Equation (27)), we limited the maximum absolute distribution difference to $\epsilon_1 = 2 \times 10^7$ Nm (around 1-2% of the maximum HF value in the validation dataset for both modes) and coefficient of variation of the MPM value to $\epsilon_2 = 0.1$ (standard deviation 10% of mean). These criteria are again more lenient than in [18] for AS, and they are applied both to AS and PAS.

3.3. Case 3 (strongly non-linear): green water impact forces

Case 3 studies a strongly non-linear problem: we predict extreme values of the green water impact forces on the front of the accommodation of the same 190 m ferry from case 2, sailing in two extreme irregular bow-quartering wave conditions (condition C and D in Table 2). The HF green water impact forces in longitudinal ship direction on the accommodation, called F''_x , were obtained from long-duration experiments. The impact forces were measured using 40 force panels on the front of the accommodation (total area 9.0×14.4 m full-scale), and F''_x is the instantaneous summation of all these measurements. Details of the HF experiments are described in [60, 70], and an overview of the test conditions is provided in Tables 1 and 2. The experimental durations were 34:49 hours (Heavy test condition) and 23:43 h (Extreme test condition). As discussed in [60], this is sufficiently long enough to have a converged HF validation reference for the half-hour MPM. Some pictures of the experiments are shown in Figure 5. The LF indicator used in this case was the relative wave elevation (RWE) at station 19 of this ship on the windward side, called R'_{19p} , generated using a linear potential flow simulation. It was shown in [18] that the pilot green water impact load case combined with AS required an LF indicator generated using coarse mesh CFD. If linear potential flow can be used instead to generate an indicator for green water impact loads (in combination with PAS), this can have a large advantage in computational time. The LF-HF peak scatter plots are shown in Appendix D. The plot shows that, as expected, the LF and HF peaks for this case have less similar order statistics than those of case 1 and 2. Again, we aim to predict the HF 30-minute MPM value $\widehat{F''_x}$ for the sailing ship. Because the experimental green water force peaks (the ground truth HF validation data) have a large tail variability, the true MPM values in Table 3 for this case were derived from a Generalised Pareto distribution fit to the 30% highest force peaks in these cases. Summarising:

- HF target extreme value: 30-minute MPM green water impact force $\widehat{F''_x}$ in the Heavy (3a) and Extreme (3b) condition.
- LF indicator: linear potential flow relative wave elevation at station 19 R'_{19p} .

To monitor convergence (see Equation (27)), we limited the maximum absolute distribution difference to $\epsilon_1 = 100$ kN (around 1-2% of the maximum HF value in the validation dataset of both conditions) and coefficient of variation of the MPM value to $\epsilon_2 = 0.05$ (standard deviation 5% of mean). Considering the lack of reliable alternative methods, a 30-minute MPM prediction with an accuracy in the order of 5% would be a very good result.



Figure 5: MARIN ferry 2 and the relevant instrumentation around the bow before the *CRS SCREAM* experiments (left), example green water impact (middle) and example bow-flare slamming impact (right).

3.4. Case 4 (strongly non-linear): bow-flare slamming forces

Case 4 studies another strongly non-linear problem, based on the same experiments as case 3. Here we predict extreme values of the bow-flare slamming forces on the same 190 m ferry from case 2 and 3, sailing in the same two extreme irregular Heavy and Extreme bow-quartering wave conditions (C and D in Table 2). The HF slamming impact forces, called F''_{p41} , were obtained from the long-duration experiments. The impact forces were measured on force panel 41 of size 1.8x1.8 cm full-scale located in the bow flare (see Figure 5). Again, details of the HF experiments are described in [60, 70], and an overview of the test conditions is provided in Tables 1 and 2. The LF indicator used for this slamming case was the same indicator as used in case 3 for green water impacts: R'_{19p} . It was suggested by e.g., [71, 72] that the rise time or rise velocity of the relative wave elevation could be more suitable as indicator for slamming loads. We also tried this, but did not find a significant improvement compared to R'_{19p} itself. To simplify as much as possible, we therefore used R'_{19p} as indicator. The LF-HF peak scatter plots are shown in Appendix D. The plot shows that the LF and HF peaks for this case have a distinctly different relation than those of the other cases. Again, we aim to predict the HF 30-minute MPM value $\widehat{F''_{p41}}$ for the sailing ship. The true HF MPM values from the experiments in Table 3 were again derived from a Generalised Pareto fit to the 30% highest force peaks. Summarising:

- HF target extreme value: 30-minute MPM bow-flare slamming force $\widehat{F''_{p41}}$ in the Heavy (3a) and Extreme (3b) condition.
- LF indicator: linear potential flow relative wave elevation at station 19 R'_{19p} .

To monitor convergence (see Equation (27)), we limited the maximum absolute distribution difference to $\epsilon_1 = 4$ kN (around 0.3% of the maximum HF value in the validation dataset of both conditions) and coefficient of variation of the MPM value to $\epsilon_2 = 0.02$ (standard deviation 2% of mean). These criteria are stricter than for the other cases, because the results kept converging very slowly. Selecting a too lenient criterion for this case would have led to less accurate results.

3.5. Implementation details for these cases

For case 1, the HF validation dataset of second-order wave elevation time traces was analytically generated with the Python PySeaWave package, using the random phase method and a frequency bandwidth of 0-5 rad/s for second-order interactions. The linear wave LF indicator time traces for case 1a were also derived from this package; the additional noise time traces for case 1b were added to this. For case 2, the HF validation dataset of non-linear VBM time traces was generated using the PRETTI_R program (v19.0.1), which is a non-linear Froude-Krylov solver using linear RAO inputs (in this case from linear frequency-domain potential flow diffraction method SEACAL). The linear VBM LF indicator time traces were also generated with SEACAL (v7.2.0) in the zero speed Green's function mode. For case 3 and 4, the HF validation datasets of green water impact forces and slamming forces were generated using experiments with a scale of 1:35.986 in the Seakeeping and Manoeuvring Basin of MARIN in Wageningen, The Netherlands. More details about these experiments can be found in [60, 70]. The linear RWE LF indicator time traces used for both cases were generated with SEACAL in the Rankine-source mode. For cases 3 and 4, the Generalised Pareto fit to the ground truth HF validation data was made using the Python `scipy.stats.genpareto` package.

4. Method used to validate PAS

In a real design procedure for a maritime structure, HF CFD simulations would need to be performed for new wave events (or a few events) at every iteration in Step 6 to obtain the required HF loads. In the present validation study, however, we circumvent this requirement: rather than running CFD simulations, we extract the corresponding HF load responses directly from a validation dataset for each selected wave event at every iteration. This allows us to focus on validating the statistical framework of the PAS method without mixing it with CFD load prediction accuracy (following the same approach used in [18] for AS). We have shown before that accurate HF wave event impact loads can be obtained with CFD (see e.g., [19, 67]). For cases 1 and 2, obtaining identical deterministic wave inputs for the LF and HF variables was straightforward. For cases 3 and 4, this was achieved by combining experimentally measured waves recorded next to the ferry, propagated to the vessel's centre of gravity, with the linear frequency-domain potential flow database of RWE response functions. This ensured that the wave phasing of the LF RWE time traces closely matched that of the experimental waves. These simulations were previously carried out for [70], where the full procedure is described in detail.

The performance of PAS relative to the validation material is assessed in terms of efficiency and accuracy using three metrics: M_1 for efficiency, and M_2 and M_3 for accuracy. M_1 (Equation (16)) is the ratio of HF samples required to reach convergence, n_c , to the total number of HF samples without PAS, n_w (the total number of wave events in the validation dataset). M_2 measures the deviation of the MPM prediction at convergence, \hat{H}_{i_c} , from the ground truth \hat{H}_t (Equation (16)), where i_c is the converged iteration number. Finally, M_3 quantifies the maximum deviation of the predicted distribution from the ground truth over a PoE range $[0.5P_{\text{exp}}, 2P_{\text{exp}}]$ (Equation (17)), with $\mathbf{h}_{\text{ran},i_c}^*(k)$ and $\mathbf{h}_{\text{t,ran}}(k)$ denoting the predicted and true distributions over this range with elements k , respectively. Smaller absolute values of all three metrics indicate better performance. Note that M_2 and M_3 may also be negative, indicating whether predictions are conservative. In theory, the convergence criteria should take care of the accuracy of the prediction. However, M_2 and M_3 are used to check whether the results converge towards the ground truth and not towards a biased value. These criteria are similar, but not identical, to those used for AS in [29].

$$M_1 = \frac{n_c}{n_w} \quad M_2 = \frac{\hat{H}_{i_c} - \hat{H}_t}{\hat{H}_t} \quad (16)$$

$$\Delta(k) = \mathbf{h}_{\text{ran},i_c}^*(k) - \mathbf{h}_{\text{t,ran}}(k) \rightarrow k^{\text{absmax}} = \arg \max_k |\Delta(k)| \rightarrow M_3 = \frac{\Delta(k^{\text{absmax}})}{\hat{H}_t}, \quad (17)$$

As explained in the introduction, PAS was based on AS. This AS method was published in [18] (with associated scripts in [30]), and fine-tuned in [29] (with associated scripts in [31]). The performance of PAS is compared to that of AS in the present publication. An overview of the steps in AS that differ from PAS and some relevant formulations are included in Appendix A. It is important to note that, throughout this study, PAS and AS are evaluated using the same analytical and linear potential-flow LF indicators. For brevity, this is not reflected in the method names; whenever AS is referenced, this indicator choice is implied. This represents a deviation from the approach used for pilot case 3 in [18], where the AS method employed an LF indicator derived from coarse-mesh CFD simulations. That AS-coarse mesh CFD combination yielded accurate distributions of green water impact loads on a containership in the pilot study.

5. Results and discussion

The resulting converged distributions from AS and PAS for all cases are presented in Figure 6 (case 1a,b), Figure 7 (case 2a,b), Figure 8 (case 3a,b) and Figure 9 (case 4a,b), together with the iterative convergence of the MPM for each case. The performance of the methods for all cases is summarised in Figure 10, using the metrics defined in Section 4. As a reminder, M_1 quantifies the efficiency of the methods relative to the HF ground-truth simulation, M_2 quantifies the deviation of the predicted HF MPM from the ground-truth MPM, and M_3 quantifies the maximum deviation between the predicted and ground-truth distributions over a range of PoE values. The ground truth for each case is always derived from the HF validation MCS datasets. The numerical values underlying Figure 10 are also included in Table 3.

These figures show that AS and PAS both provide accurate MPM and distribution predictions for all variations of cases 1 and 2. This was also demonstrated in [18] for AS. However, the results obtained using AS with the USMV acquisition function were slightly more accurate than the present AS with MVPD results for case 2a. M_2 in Figure 10

Design loads for wave impacts

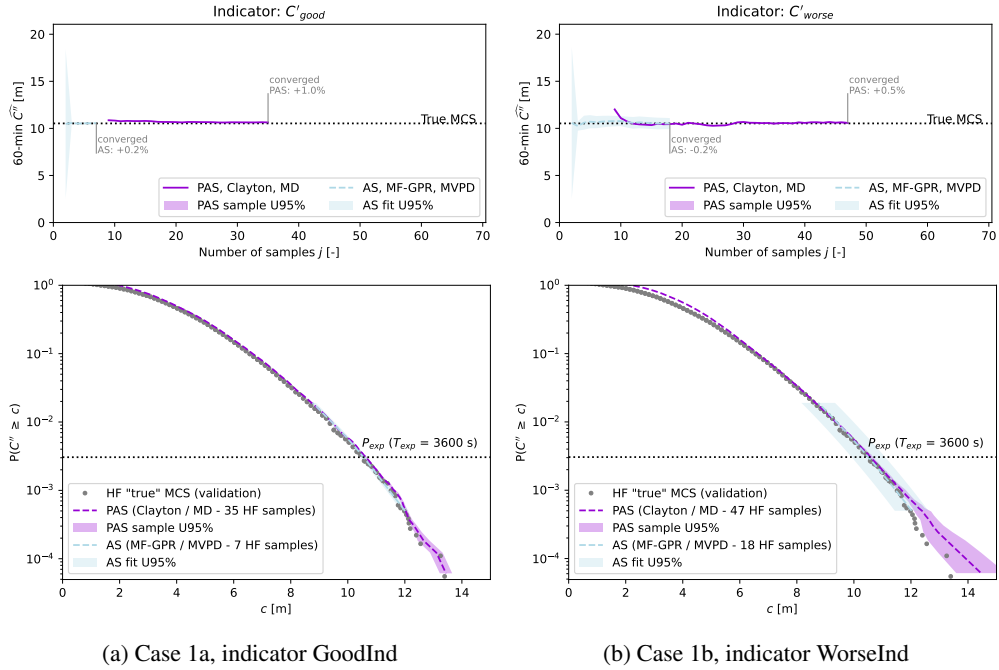


Figure 6: Case 1 - waves: convergence of one-hour MPM as a function of number of samples (top) and final converged distributions (bottom) from AS and PAS. The copula in the name of the PAS results is the used model in the last iteration.

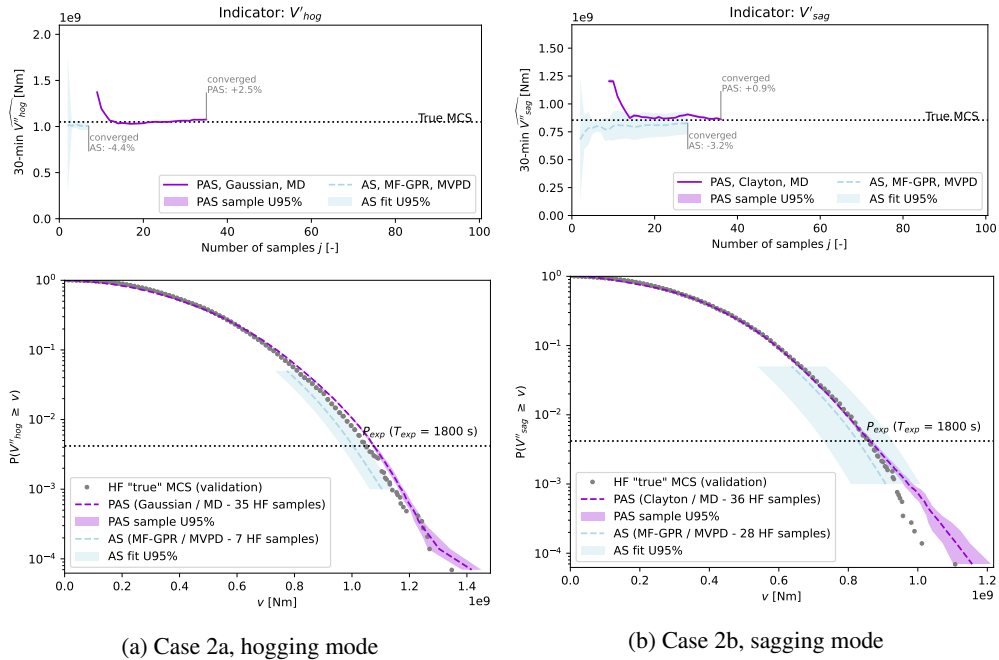


Figure 7: Case 2 - VBM: convergence of one-hour MPM as a function of number of samples (top) and final converged distributions (bottom) from AS and PAS. The copula in the names of the PAS results is the used model in the last iteration.

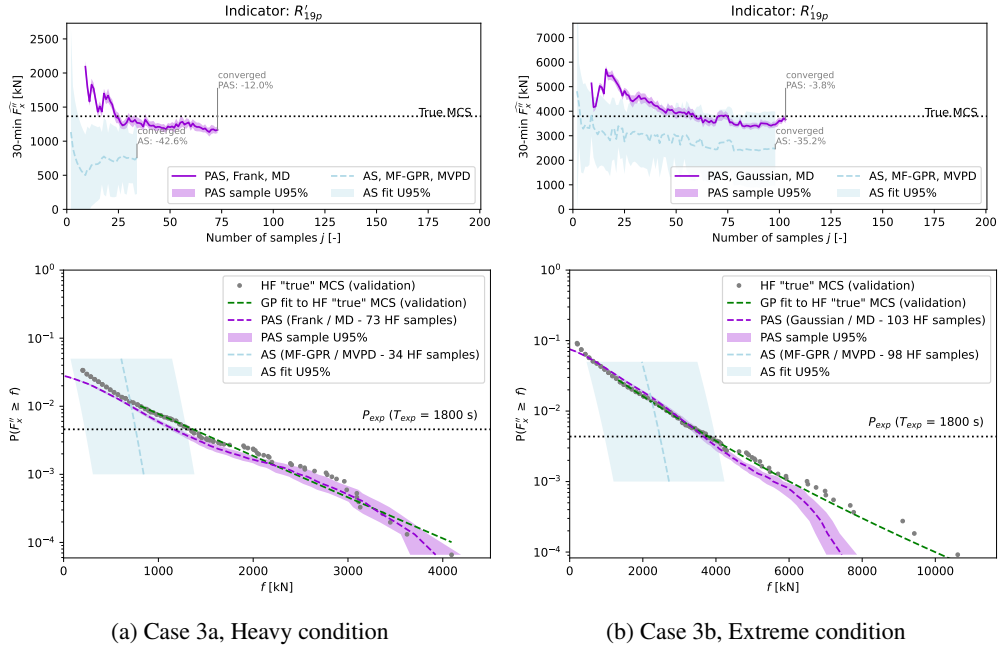


Figure 8: Case 3 - green water: convergence of one-hour MPM as a function of number of samples (top) and final converged distributions (bottom) from AS and PAS with indicator R'_{19p} , where GP fit = Generalised Pareto fit to 30% highest true validation peaks. The copula in the name of the PAS results is the used model in the last iteration.

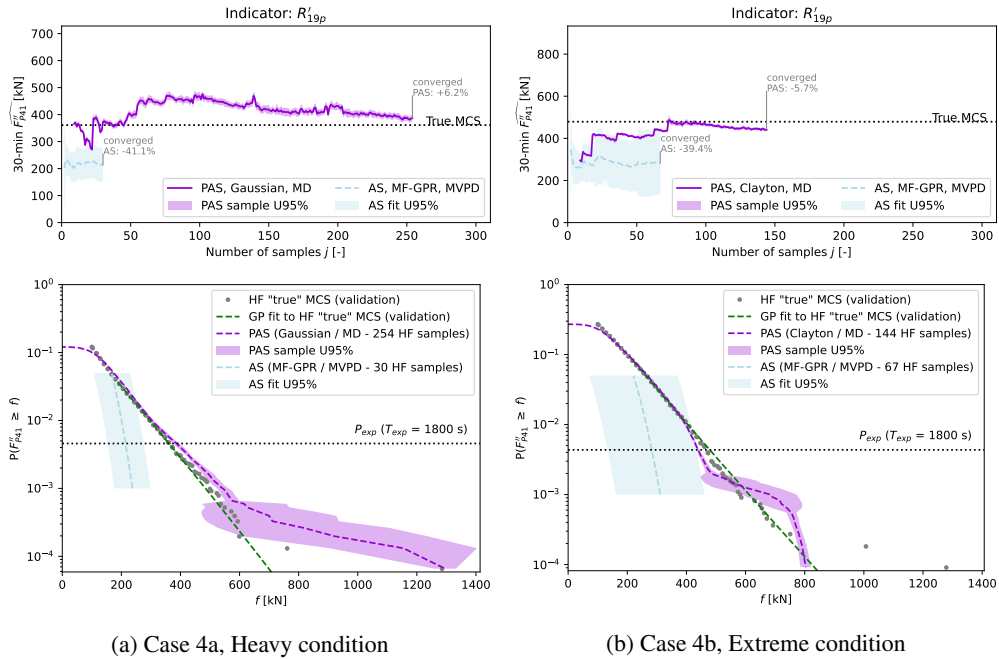


Figure 9: Case 4 - slamming: convergence of one-hour MPM as a function of number of samples (top) and final converged distributions (bottom) from AS and PAS with indicator R'_{19p} , where GP fit = Generalised Pareto fit to 30% highest true validation peaks. The copula in the name of the PAS results is the used model in the last iteration.

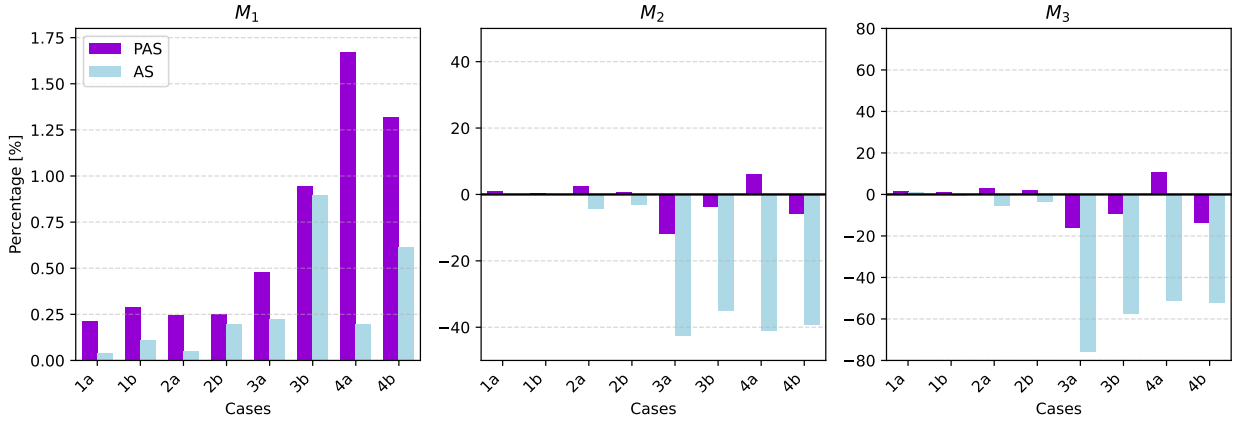


Figure 10: Performance metrics M_1 , M_2 and M_3 defined in Section 4 for all considered cases.

shows that both methods produce MPM results with accuracy well within 5% for these two cases, which is acceptable for design purposes. However, the results for cases 3 and 4 clearly highlight the advantage of PAS over AS combined with linear potential flow. The inclusion of probabilistic copula fitting in PAS significantly reduces the bias introduced by the quality of the screening indicator in AS. The M_2 values show that PAS is able to predict the target extreme MPM values with an accuracy within 10% for all variations of cases 3 and 4, whereas AS shows deviations of up to 40%. The figure also clearly shows the inherent non-conservative tendency of AS (which is problematic for design load estimation). This trend is not present in the results from PAS; the small deviations observed in the MPM and the distributions can be either conservative or non-conservative. Similar results are observed for M_3 , which highlights that the maximum deviations of the PAS distributions compared to the ground truth are within 18% for all test cases, and those of AS within almost 80%. It should be kept in mind that the present results rely on combining both PAS and AS with linear potential flow indicators. [18] demonstrated that AS, when combined with a coarse-mesh CFD indicator, can yield accurate green water load distributions. However, obtaining indicators from 3D coarse-mesh CFD is far more computationally expensive than using linear potential flow, which highlights the advantage of PAS over AS.

When comparing the extreme values from the validation datasets with those obtained using (P)AS, the respective uncertainties of these values must be considered. The distributions in Figures 6 to 9 also show the U95% MF-GPR uncertainty for AS, and the U95% sample uncertainty based on 20 draws from the fitted copula model for PAS. These uncertainty measures are not directly comparable, but they show that the sample uncertainty from PAS is small around P_{exp} for all eight case variations (whereas the MF-GPR uncertainty band from AS is larger around P_{exp}). For case 1, the HF validation sample uncertainty is 0.1 m ($\sim 1\%$ of the true MPM value, see Table 3 and [18]). The U95% uncertainty of the PAS results is 0.06 m (case 1a) and 0.21 m (case 1b), which corresponds to $\sim 0.6\%$ and $\sim 2\%$ of the true MPM values, respectively. For case 3, the root-mean-square sample errors (RMSE) of the extreme values in the HF validation data are discussed in detail in [60], showing that these converge to well below 100 kN for the 30-minute MPM in both test conditions. This roughly translates² to an U95% uncertainty around 200 kN ($\sim 7\text{--}15\%$ of the true MPM values). The U95% uncertainty of the PAS results is 96 kN (case 3a) and 292 kN (case 3b), which corresponds to $\sim 7\%$ and $\sim 10\%$ of the true MPM values, respectively. The uncertainty of the extreme values in the HF validation data was not evaluated for cases 2 and 4, but it is expected to be between case 1 and 3 for case 2, and comparable to case 3 for case 4. The validation uncertainties reported above for cases 1 and 3 relate to the sample variability over many different realisations of the same wave condition. This does not relate directly to the present validation, as we reproduced the same wave realisation with the LF tools (see Section 4). We should therefore consider the repetition uncertainty of the experimental results in case 3. We do not have this information directly, but we know from e.g., [73] that this uncertainty can be in the same order as the sample variability for wave impacts measured in a seakeeping basin. Based on this, both the experimental and PAS uncertainties are considered to be sufficiently small for all cases to make the validation comparison meaningful.

²Assuming a normal distribution, RMSE is equal to standard deviation error, and $\text{U95\%} \approx 1.96 \text{ RMSE}$.

Design loads for wave impacts

	Case 1a	Case 1b	Case 2a	Case 2b	Case 3a	Case 3b	Case 4a	Case 4b
Predicted MPM at convergence for case-specific T_{exp}								
HF MCS*	10.53 m (U95% 0.10 m)		1.05×10^9 Nm	8.55×10^8 Nm	1.37×10^3 kN	3.79×10^3 kN	361 kN	479 kN
AS	10.55 m	10.51 m	1.00×10^9 Nm	8.27×10^8 Nm	0.76×10^3 kN	2.47×10^3 kN	214 kN	283 kN
PAS	10.64 m	10.58 m	1.08×10^9 Nm	8.62×10^8 Nm	1.17×10^3 kN	3.66×10^3 kN	387 kN	440 kN
Required number of HF samples for convergence								
HF MCS (all waves)	16364	16364	14359	14359	15198	10900	15198	10900
AS	7	18	7	28	34	98	30	67
PAS	35	47	35	36	73	103	254	144
LF duration to simulate (analytical / linear potential flow)								
HF MCS	-	-	-	-	-	-	-	-
AS	50 h	50 h	30 h	30 h	34:49 h	23:43 h	34:49 h	23:43 h
PAS	50 h	50 h	30 h	30 h	34:49 h	23:43 h	34:49 h	23:43 h
HF duration to simulate (CFD / experiments)								
HF MCS	50 h	50 h	30 h	30 h	34:49 h	23:43 h	34:49 h	23:43 h
AS (estimate**)	~2 min	~6 min	~2 min	~9 min	~11 min	~33 min	~10 min	~22 min
PAS (estimate**)	~12 min	~16 min	~12 min	~12 min	~24 min	~34 min	~85 min	~48 min

* Ground truth.

** Assuming HF events with a duration of 20 s each as discussed in Section 5.

Table 3

Summary of the results for all cases (more details about the cases themselves can be found in Table 1), where 'HF MCS' refers to the present validation datasets.

When accuracy would be the only indicator for the performance of an extreme value prediction method, MCS would always be preferred. The objective of (P)AS is to make accurate predictions *in a more efficient way*. M_1 in Figure 10 shows that both methods significantly reduce the required number of HF samples that need to be evaluated compared to the HF validation data: the number of wave events to evaluate with an HF tool is below 1.7% compared to those required in the MCS for all cases and both AS and PAS. The figure also shows that AS is consistently more efficient than PAS when combined with potential flow indicators. However, [18] demonstrated that using the coarse-mesh CFD indicators required to obtain accurate results for the more complex cases substantially reduce the efficiency of AS. Still, it can be interesting to use AS with potential flow for relatively simple problems such as cases 1 and 2, where it can provide accurate results, and quicker than PAS. PAS is the more reliable method for accurate and efficient predictions across all cases, particularly the complex ones. PAS needs evaluation of less than 0.3% of the HF events compared to MCS for case 1a,b and 2a,b, and less than 1.7% of the HF events compared to MCS for case 3a,b and 4a,b. The exact number of required events depends on the limits set for the stopping criteria. These were defined per case in the present study; the optimal stopping limits for a new case depend on the designer's requirements, acceptable risks, considered quantiles, and probably requirements by class societies.

In all cases, this is a considerable reduction in the required number of HF events to simulate compared to MCS, or to conventional experimental approaches (as discussed in [18]). However, to assess whether the full PAS procedure is feasible during the design stage of a new vessel, these numbers need to be translated to simulation durations. As explained in Section 4, we focused the validation on the statistical framework and did not perform the CFD calculations for the selected HF events. We can therefore only estimate the required durations. As also discussed in [18], there is a substantial body of literature showing that HF CFD can accurately replicate wave impact loads when it accurately reproduces the wave and ship motion data from experiments. The duration per event varies in these studies, ranging from $4T_p$ [74], 50 s [75], 35 s [65], ~20 s [19], to even as short as 3 s [66]. There are also studies that initialise the CFD simulations from a LF tool instead of experiments (as done in a screening method); this can be done with 52 s [76] or 12 s [67] event durations. When fully non-linear wave-event kinematics near the structure and the corresponding ship motions are available from the LF tool, only a short simulation duration is needed. In contrast, if the waves and motions must be initialised from linear wave elevations or at locations further from the structure, a longer duration may be necessary. In our study, it is reasonable to assume that the waves in CFD can be initialised close to the structure (as discussed in more detail below), and that the ship motions can be imposed from the linear potential flow simulations. This should make it possible to reduce the duration per HF event to ~20 s (following the procedure in the green water impact study [19]). Using this assumption, we can translate the required number of HF events to HF simulation durations (see Table 3). This results in total durations to simulate with HF CFD in the order of 2 to 85 minutes, which seems feasible in the design stage of a ship. In comparison, the HF validation datasets used between 23 and 50 hours of HF experiments. The PAS requirements correspond to between 0.1% and 4% of the HF MCS durations across all cases. Note that these percentages are roughly twice the M_1 values, because with typical wave periods of around 10 s, a

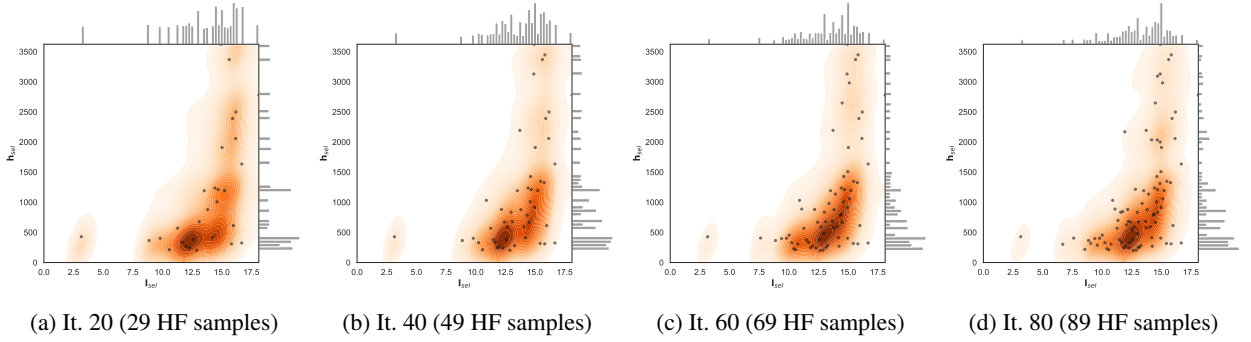


Figure 11: Fitted copula models (and the histogram of the associated marginals) at different iteration numbers for green water case 3a from the full PAS procedure, where it. = iteration. This case was converged with 73 HF samples.

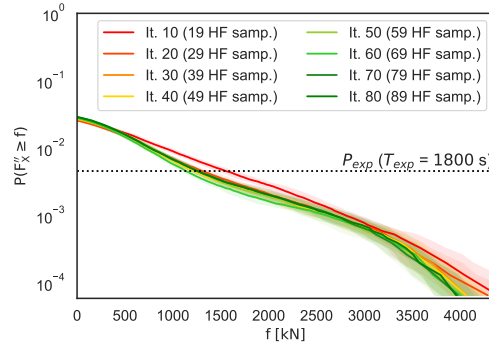


Figure 12: Predicted distributions at different iteration numbers for green water case 3a from the full PAS procedure.

20 s event corresponds to two wave encounters. The computational time required for these simulations (in CPU hours) also depends on the CFD tool used, as well as the chosen grid size, domain, and time-step settings for each case.

Because the results of PAS partly depend on the fitted copula, and because this part of the method is different from AS, we provide some insight into the influence of the fitted copula in [Appendix E](#). This demonstrates that it is not necessary to wait for the procedure to converge to the ‘true’ copula model. Instead, the most likely copula model among the four candidates already provides a sufficiently accurate estimate to produce reliable distribution predictions, and it does so using fewer HF samples than full convergence of the copula model would require. This is supported by [Figure 11](#) (evolution of HF samples and fitted copula model with an increasing number of iterations for case 3a) and [Figure 12](#) (evolution of predicted distributions for the same case). These plots show that the distributions already converge to accurate results with the Frank copula, even though [Figure 14](#) in the appendix shows that the Gumbel copula may fit the full HF validation dataset better.

As noted in [Section 2.1](#), initialising HF event simulations in [Step 6](#) of PAS using the LF screening results is not straightforward. In this paper, we bypassed this challenge by selecting HF events from the validation dataset rather than performing the CFD calculations. However, for applying PAS to a new ship design, a method to initialise HF simulations from LF output will be required. There is no universally accepted and statistically sound way to correlate linear (or weakly non-linear) wave events with equivalent fully non-linear wave events. Still, we need to define input conditions for the HF CFD calculations or experiments, based on the selected LF wave events. Potential solutions for this include event matching procedures as discussed by [74, 77], or using coarse mesh CFD as an LF tool (see e.g., [67]). The first method may be useful for offshore structures but less for sailing ships, and the second method requires relatively expensive coarse mesh CFD as LF screening tool (as demonstrated in combination with AS in [18]). A potential alternative approach involves first performing MCS with a fully non-linear wave-only tool (such as a higher-order spectral method, HOS) as in [Step 2](#), followed by linear potential flow screening applied to the resulting wave time trace. When LF events are subsequently selected in [Step 5](#) or [Step 11](#) and evaluated with a HF tool in

Step 6, the HF simulation for each event could be initialised using the corresponding HOS simulation. However, this initialisation approach requires further investigation, which is beyond the scope of the present study.

As noted in Section 1.4, the present study only validates PAS in a short-term extreme value setting. In a future real application, we also need to select sea states and handle their long-term statistics properly. In theory, this can be done using PAS as well. Alternatively, a version of the environmental contour method, as described in [78] or [79, 80], could be used. This approach is widely accepted in the offshore industry (e.g., [21]), though it can sometimes fail to accurately characterise the joint distribution of environmental variables [81–83]. Another option is to use another adaptive sampling method, as proposed by [84, 85].

6. Conclusions

Based on the present work, it can be concluded that the newly proposed extreme value prediction method PAS provides accurate estimates of the short-term distributions and extreme values compared to the available full brute-force MCS datasets for a range of validation cases. The method introduces a probabilistic approach to multi-fidelity screening, allowing efficient linear potential flow indicators to be used in the low-fidelity stage, even for strongly non-linear load cases. PAS achieves a most probable maximum (MPM) accuracy within 10% for all considered cases in the present study, including variations of non-linear waves, vertical bending moments, green water impact loads, and slamming loads. In addition, PAS achieves this performance very efficiently, requiring less than 4% of the high-fidelity simulation time needed for conventional MCS for all cases. While PAS is similarly accurate and slightly less efficient than its predecessor AS for the simpler cases (non-linear waves and vertical bending moments), it proves significantly more reliable for the more complex cases (green water and slamming loads). These results demonstrate that PAS can reliably reproduce the statistics of both weakly and strongly non-linear extreme load problems, while significantly reducing the associated computational cost. The present study validates the statistical PAS framework; further work should focus on validating the full procedure including CFD load simulations, and on validating it for long-term extremes.

Acknowledgements

This publication is part of the project “Multi-fidelity Probabilistic Design Framework for Complex Marine Structures” (project TWM.BL.019.007) of the research programme “Topsector Water & Maritime: the Blue route” which is (partly) financed by the Dutch Research Council (NWO). The authors thank the Cooperative Research Ships (CRS) for permitting us to use the PySeaWave package, the SEACAL and PRETTI_R programs, and the experimental data in case 3 and 4. The authors also thank Cees de Valk of KNMI for suggesting copula modelling as a way to reduce bias in sampling methods.

Data availability

All scripts underlying this publication and the datasets of case 1 and 2 are available in the 4TU repository: [68]. The full datasets underlying cases 3 and 4 are proprietary (owned by the CRS).

Appendices

A. Details of the Adaptive Screening (AS) method

Here, the steps of AS are briefly summarised. This is a shortened reproduction of the full description and formulations in [18]. Steps 1 to 6 of AS are identical to Step 1 to Step 6 described in Section 2.1. The next three steps are different. They are described here in general terms (for details, see [18]). **Step 7** estimates the sample HF distribution, by assuming that the order statistics of \mathbf{l}^{sel} and \mathbf{h}^{sel} are identical. This is a critical screening assumption that only works if a suitable indicator signal is chosen. It indicates that the HF distribution $[\mathbf{d}_H^{\text{sel}}, \mathbf{h}^{\text{sel}}]$ can be estimated using $\mathbf{d}_H^{\text{sel}} \approx \mathbf{d}_L^{\text{sel}}$. **Step 8** defines a range \mathbf{d}^* of PoE between 1 and 0 around P_{exp} , over which to estimate the HF distribution. **Step 9** constructs the surrogate HF distribution \mathbf{h}^* over $\ln(\mathbf{d}^*)$ using single- or multi-fidelity Gaussian Process Regression (GPR). With single-fidelity GPR, we use the HF sample dataset $[\ln(\mathbf{d}_H^{\text{sel}}), \mathbf{h}^{\text{sel}}]$ as input. With

multi-fidelity MF-GPR, we use the same HF sample dataset $[\ln(\mathbf{d}_H^{\text{sel}}), \mathbf{h}^{\text{sel}}]$ as input, and LF dataset $[\ln(\mathbf{d}_L^{\text{mcs}}), \mathbf{l}^{\text{mcs}}]$ from Step 3. After that, steps 10 to 12 of AS are identical to Step 10 to Step 12 of PAS again. Similarly as explained for PAS in Section 2.4, AS used an acquisition function to obtain one new HF sample in every iteration. In [18], we employed an acquisition function that balanced selecting samples based on the uncertainty band of the previous iteration and drawing from the upper tail (function *USMV*). In [29], we explored variations of this acquisition strategy and concluded that a function that balances sampling around the acceptable probability level with upper-tail sampling is more efficient (function *MVPD*). The latter function is used in the present study for AS, combined with MF-GPR. This is formulated in Equation (18), where $\bar{\mathbf{h}}_n^*$ is the normalised mean HF distribution prediction from the previous iteration. Similar as in PAS, the closest sample from the available MCS pool is then selected, and the new sample is added to the existing LF pool of samples for the next iteration.

$$p_{\text{new}}^{\text{mvpd}} = \arg \max \left[\bar{\mathbf{h}}_n^* \cdot \left(\frac{\mathbf{f}_2}{\max(\mathbf{f}_2)} \right) \right] \quad \text{where:} \quad \begin{cases} \mathbf{f}_1 = 1 - (\ln(\mathbf{d}^*) - \ln(P_{\text{exp}}))^2 \\ \mathbf{f}_2 = \mathbf{f}_1 - \min(\mathbf{f}_1) \end{cases} \quad (18)$$

B. Copula basics

B.1. General theory

Copulas were introduced by Abe Sklar in 1959 [86]. They are multivariate distribution functions with uniform marginals on the interval $[0, 1]$. Let F be a joint cumulative distribution function (CDF) with marginals F_1, F_2, \dots, F_d . Then there exists a copula C defined in Equation (19). If the marginals are continuous, then the copula C is unique and can be written as Equation (20) (Sklar's theorem).

$$F(x_1, x_2, \dots, x_d) = C(F_1(x_1), F_2(x_2), \dots, F_d(x_d)) \quad (19)$$

$$C(u_1, u_2, \dots, u_d) = F(F_1^{-1}(u_1), F_2^{-1}(u_2), \dots, F_d^{-1}(u_d)) \quad (20)$$

Copulas are widely used in finance, hydrology, engineering, and related fields to model dependence between random variables. Their main advantage is the separation of marginal distributions from the dependence structure, allowing flexible and accurate modelling of joint behaviour (especially for tail-dependent data). Compared to empirical joint distributions, which require large sample sizes, copulas offer a more efficient framework. They enable robust interpolation and extrapolation of joint behaviour, even in regions where data is sparse and empirical methods fail. This makes them valuable for surrogate modelling, uncertainty quantification, and extreme value analysis in multivariate or multi-fidelity settings. A helpful analogy for hydrodynamicists is the common practice of fitting theoretical univariate distributions to experimental data (e.g., GEV or Weibull) to enable reliable interpolation and extrapolation of the extremes. Copulas offer similar benefits. They are also associated with similar risks. Poor fits can lead to misleading extreme value predictions. A well-known example is the 2008 financial crisis, where underestimated tail dependence in loan portfolios contributed to large failures (see e.g., [87]). Ensuring a good fit, particularly in the tails, is therefore essential when using copulas to model extremes.

Dependence in the lower and upper tails of any copula is measured using the lower / upper tail dependence coefficients λ_L and λ_U , respectively. An upper tail dependence coefficient $\lambda_U = 0.81$ means that there is a 81% chance that if one variable is in the extreme upper tail, the other is too. A measure for the overall dependence of two variables is *Kendall's tau* τ . This can be estimated from an empirical distribution, after which it can be used to estimate the copula parameters using the formulations below.

B.2. Copula families and formulations

Several copula families exist, most of which belong to the two main classes: *elliptical* and *Archimedean* copulas. Elliptical copulas are derived from elliptical distributions (e.g., the multivariate normal or *t*-distribution); they are symmetric and mainly capture linear or elliptical dependence. An example is the Gaussian copula used in this study. Archimedean copulas form a flexible family defined through a generator function φ in $C(u, v) = \varphi^{-1}(\varphi(u) + \varphi(v))$. They can be used to model various types of tail dependence. The Clayton, Gumbel, and Frank copulas applied here belong to this class. Although copulas can model dependence among multiple variables, we use only their bivariate forms. The **Gaussian** copula is derived from the multivariate normal distribution and is defined in Equation (21), where Φ denotes the standard normal CDF and Φ_ρ the joint CDF of a bivariate standard normal distribution with correlation ρ . This

copula has a single parameter $\rho \in [-1, 1]$, equal to the Pearson correlation coefficient. The Gaussian copula models symmetric dependence but has no tail dependence, meaning its tail dependence coefficients are $\lambda_L = \lambda_U = 0$. This does not mean that there is no dependence in the tails, but that dependence weakens rapidly in the extremes, and joint extremes are not more likely than implied by the overall correlation. Parameters ρ and τ are related: $\tau = \frac{2}{\pi} \arcsin(\rho)$. The **Clayton** copula captures lower tail dependence. It is defined in Equation (22), where $\theta \in (0, \infty)$ measures the strength of the dependence. The lower tail dependence coefficient is related to the Clayton parameter: $\lambda_L = 2^{-1/\theta}$. There is no upper tail dependence ($\lambda_U = 0$), and $\tau = \theta/(\theta + 2)$. The **Gumbel** copula captures upper tail dependence. It is defined in Equation (23), where $\theta \in [1, \infty)$ again measures the strength of the dependence. The upper tail dependence coefficient is related to the Gumbel parameter: $\lambda_U = 2 - 2^{1/\theta}$. There is no lower tail dependence ($\lambda_L = 0$), and $\tau = 1 - 1/\theta$. The **Frank** copula is symmetric, without tail dependence. It is defined in Equation (24), where θ can be any real number except 0, $\theta > 0$ means positive dependence, and $\theta < 0$ means negative dependence. There is no tail dependence in the Frank copula ($\lambda_L = \lambda_U = 0$), and $\tau = 1 - 4/\theta (1 - D_1(\theta))$, where $D_1(\theta)$ is the Debye function: $D_1(\theta) = 1/\theta \int_0^\theta t/(e^t - 1) dt$.

$$C_\rho^{\text{gaussian}}(u, v) = \Phi_\rho(\Phi^{-1}(u), \Phi^{-1}(v)) \quad (21)$$

$$C_\theta^{\text{clayton}}(u, v) = (u^{-\theta} + v^{-\theta} - 1)^{-1/\theta}, \quad \theta > 0. \quad (22)$$

$$C_\theta^{\text{gumbel}}(u, v) = \exp\left(-[(-\ln u)^\theta + (-\ln v)^\theta]^{1/\theta}\right), \quad \theta \geq 1. \quad (23)$$

$$C_\theta^{\text{frank}}(u, v) = -\frac{1}{\theta} \ln\left(1 + \frac{(e^{-\theta u} - 1)(e^{-\theta v} - 1)}{e^{-\theta} - 1}\right), \quad \theta \in \mathbb{R} \setminus \{0\}. \quad (24)$$

C. PAS stopping criterion

The stopping criterion in PAS has two components: one monitors the convergence of the predicted distribution shape, and the other monitors the convergence of the resulting MPM value. The first component is based on the mean absolute difference $E(j)$ between successive predicted distributions over a PoE range, $\mathbf{h}_{\text{ran}}^*(j-1)$ and $\mathbf{h}_{\text{ran}}^*(j)$ for iteration j . This range is taken between $P_{\text{exp}}/2$ and $P_{\text{exp}} \cdot 2$, to focus on the distribution shape around P_{exp} . Part one of the stopping criterion $\bar{E}_{K_1}(j)$ is then defined in Equation (25), by taking the average $E(j)$ over the last K_1 iterations. This is done to ensure a smooth convergence. When $j < K_1$, all available iterations are used, but we set a convergence threshold at $K_1/2$ (convergence can only be declared after this number of iterations).

$$\bar{E}_{K_1}(j) = \frac{1}{\psi} \sum_{i=\chi}^j E(i) \quad \text{where:} \quad \begin{cases} E(j) = \text{mean} |\mathbf{h}_{\text{ran}}^*(j) - \mathbf{h}_{\text{ran}}^*(j-1)| \\ \chi = 1 \text{ and } \psi = j & \text{for } j = 1, 2, \dots, K_1 - 1 \\ \chi = j - K_1 + 1 \text{ and } \psi = K_1 & \text{for } j \geq K_1 \end{cases} \quad (25)$$

The second part is based on a convergence criterion on the coefficient of variation (COV) of the MPM value over the last K_2 iterations: $C_{K_2}(j)$. This is expressed in Equation (26), where $\hat{H}(j)$ is the MPM value predicted in iteration j . Again, we took the COV over the available iterations when $j < K_2$.

$$C_{K_2}(j) = \frac{\sigma_{K_2}(j)}{\mu_{K_2}(j)} \quad \text{where:} \quad \begin{cases} \mu_{K_2}(j) = \frac{1}{\psi} \sum_{i=\chi}^j \hat{H}(i) \\ \sigma_{K_2}(j) = \sqrt{\frac{1}{\psi} \sum_{i=\chi}^j (\hat{H}(i) - \mu_{K_2}(i))^2} \\ \chi = 1 \text{ and } \psi = j & \text{for } j = 1, 2, \dots, K_2 - 1 \\ \chi = j - K_2 + 1 \text{ and } \psi = K_2 & \text{for } j \geq K_2 \end{cases} \quad (26)$$

The total stopping criterion $S(j)$ is provided in Equation (27), where limits ϵ_1 and ϵ_2 are case-dependent, and where $K_1 = K_2 = 50$ limit the influence of outliers and the minimum number of iterations for which convergence can be detected.

Design loads for wave impacts

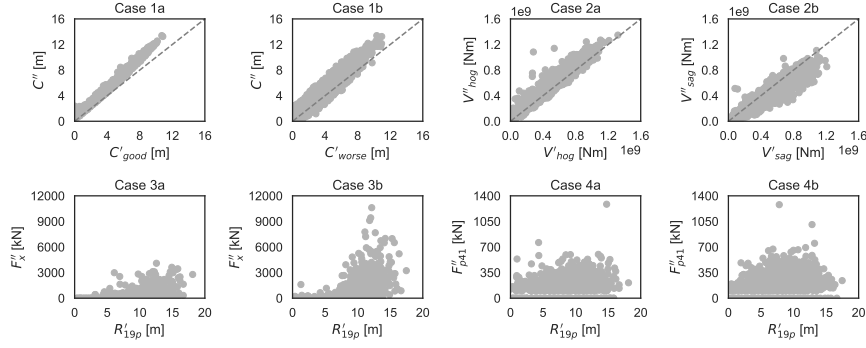


Figure 13: Scatter plots of LF indicator peaks and matched HF validation peaks for all cases.

$$S(j) = \begin{cases} \text{stop} & \text{if } (\overline{E}_{50}(j) < \epsilon_1) \cap (C_{50}(j) < \epsilon_2) \\ \text{continue} & \text{otherwise} \end{cases} \quad (27)$$

Compared to the stopping criterion used for AS in [18], we removed the rejection criterion for distribution shapes that violate distribution assumptions (as drawing from the copula model in Step 8 of PAS always produces a proper distribution), we added a range over which Equations (25) and (26) are calculated (this was natural in AS because most steps considered such a range, but not in PAS), we used the mean absolute difference instead of the maximum absolute difference in Equation (25), we used $K_1 = K_2 = 50$ instead of 20 (to ensure smoother convergence), and we added the convergence threshold.

D. LF-HF scatter plots

The scatter plots of LF indicator peaks and the corresponding matched HF response peaks from the validation material are plotted for all cases in Figure 13. This relation is not known in the design stage of a new ship, but it is available from the HF validation material for the cases in the present study. These plots illustrate the validity of the screening assumption that the order statistics of the LF and HF peaks are comparable. If the order statistics were exactly identical, all samples would lie on a single, monotonically increasing line in both x and y. Instead, the plots show that the test cases span a range of LF-HF pairs, from cases that satisfy the assumption almost perfectly to cases that do so only approximately.

E. Influence of copula fitting on the results

First, we evaluate how the iterative copula selection procedure converges for all considered cases (Appendix E.1). Next, we discuss how the predicted distributions depend on the selected copula models (Appendix E.2)

E.1. Convergence of copula selection

The selection procedure of the copula model in Step 7 of PAS is explained in Section 2.2. It is based on the log-likelihood of the four candidate copulas compared to the HF samples in the considered iteration. The aim of this exercise is not to prove which copula model fits the full validation dataset best; it is to evaluate which copula suits the presently available set of HF samples the best. It is therefore not necessarily required that this converges to one single copula model for each case; new insight gained in the Bayesian adaptive sampling procedure from the newly added HF samples may change which model is most likely.

How this works out is visualised by the log-likelihood in one case (green water case 3a) as a function of the number of iterations, as shown in Figure 14. This figure shows that the Gumbel copula is most likely for the first few iterations, after which the Frank copula is most likely up to around 150 HF samples and the Gumbel copula again after that. Section 5 shows that the predicted distribution for this case was considered converged and quite accurate at 73 HF samples already. It is therefore not necessary to arrive at a ‘true copula model’ before predicting the distributions; the most likely model with fewer HF samples already produces a good enough result. For completeness, Figure 15

Design loads for wave impacts

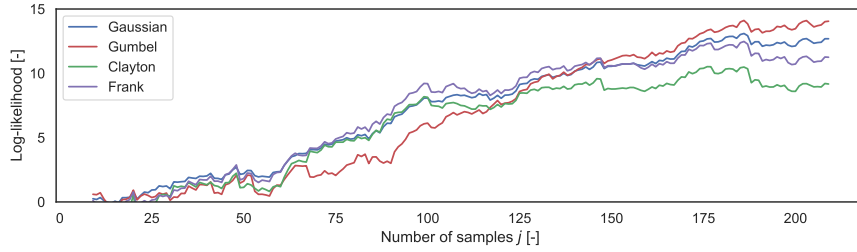


Figure 14: Log-likelihood of the four copula candidate models as a function of the number of HF samples, for green water case 3a (which is converged at 73 HF samples).

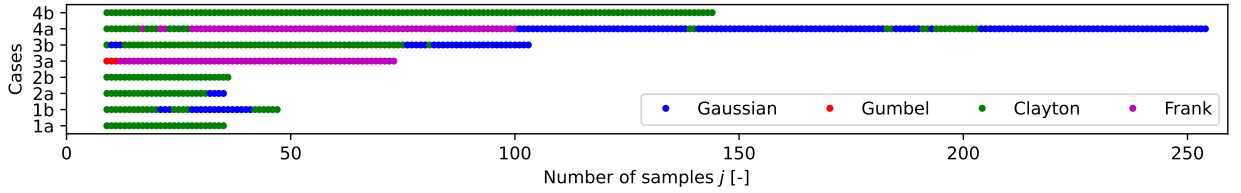


Figure 15: Selected copula per case and iteration, plotted until convergence in each case.

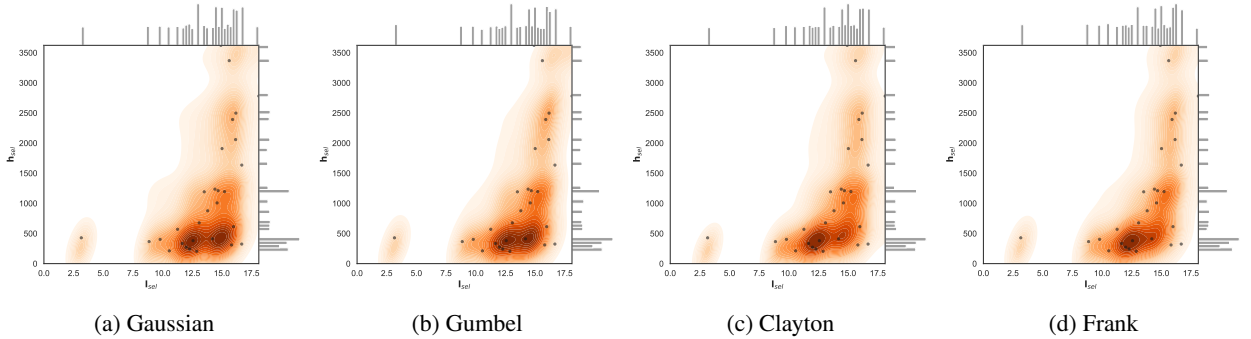


Figure 16: Different fitted copula models (and the histogram of the associated marginals) to the HF samples generated with the full PAS procedure at 20 iterations (29 HF samples, not converged yet), for green water load case 3a.

provides an overview of the most likely copula models for each case and each iteration (up to a number of iterations past convergence).

E.2. Influence of selected copula model on results

For a given set of HF sample data in one of the iterations of PAS, the predicted distribution depends to some extent on the fitted copula model in that iteration. To evaluate how large the influence of this copula choice can be on the results, we dive into this for one case (green water case 3a). Figure 16 plots the 29 HF samples generated with the PAS procedure for this case at 20 iterations (the procedure is not yet converged at that point), together with all four candidate copula models fitted to these samples. This shows that the shape of the fitted copula models looks very similar. However, Figure 17a shows that the tail of the distributions drawn from these models can be significantly different for 20 HF samples. Selecting the most-likely copula model per iteration instead of *a priori* selecting one model can therefore pay off in the prediction of the extremes. The same distribution with the copula models fitted to 100 HF samples for the same case in Figure 17b shows that the difference in the upper tail reduces with an increasing number of samples. In other words, for a large number of samples, all copula models seem to converge to a similar distribution. Around P_{exp} , the differences are especially small with 100 HF samples.

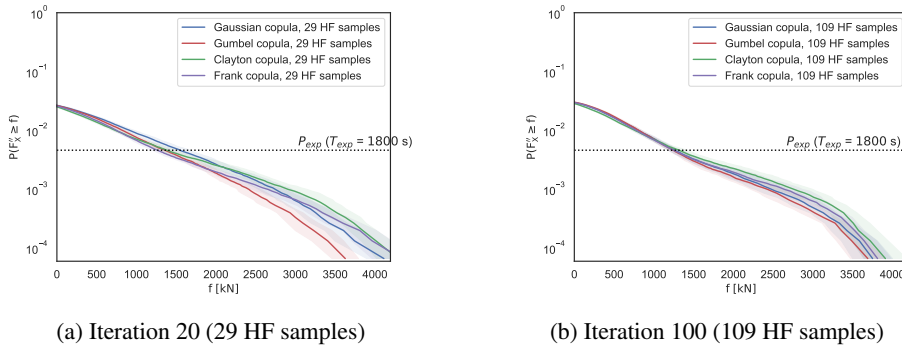


Figure 17: Exceedance probability distributions (mean and 95th percentile) resulting from 20 draws of each of the four copulas fitted to the 29 HF samples from iteration 20 and 100, for green water load case 3a.

Declaration of generative AI / AI-assisted technology in the manuscript preparation process

During the preparation of this work the authors used ChatGPT in order to rephrase a few individual sentences. After using this tool/service, the authors reviewed and edited the content as needed and take full responsibility for the content of the published article.

References

- [1] R. P. Dallinga, G. Gaillard, Hatch cover loads experienced by M.V. Derbyshire during typhoon ‘Orchid’, in: Glasgow Marine Fair And Int. Workshop On Safety Of Bulk Carriers, Glasgow, Scotland, UK, 2001.
- [2] G. K. Kapsenberg, On the slamming of ships, PhD thesis, Delft University of Technology, Delft, The Netherlands (2018). doi:10.4233/uuid:14eac2bb-63ee-47e4-8218-1ba3830a97b4.
- [3] I. Pereira, Coast Guard probing deaths, injuries of Americans on vessels in Antarctic waters, ABC News (2023).
- [4] Reuters, Norwegian cruise ship MS Maud loses power in North Sea during storm, The Guardian (2023).
- [5] M. Halsne, O. N., G. Ersdal, M. Langoy, T. Andersen, L. G. Bjørheim, Semisubmersible in service experiences on the Norwegian Continental Shelf, in: 41th OMAE Conf., ASME, Hamburg, Germany, 2022. doi:10.1115/OMAE2022-81289.
- [6] G. Ersdal, A. Kvitrud, Green water on Norwegian production ships, in: 10th ISOPE Conf., Int. Soc. of Offshore and Polar Eng. (ISOPE), Seattle, USA, 2000.
- [7] N. Zhang, L. Xiao, Q. Zou, C. Cummins, Large-scale wave basin experimental study on the spatio-temporal distribution of wave impact loads on a semi-submersible platform, Ocean Eng. 327 (2025) 120991. doi:10.1016/j.oceaneng.2025.120991.
- [8] I. Viste-Ollestad, T. L. Andersen, N. Oma, S. Zachariassen, Investigation report Petroleumstilsynet - Investigation of an accident with fatal consequences on COSLInnovator, 30 December 2015, Tech. rep. (2016).
- [9] Norwegian Ocean Industry Authority Havtil, Investigation of incident on 31 January 2024 involving a cabin window on Åsgard A being forced in by green water, Tech. rep. (2025).
- [10] G. Cuomo, G. Lupoi, K. Shimosako, S. Takahashi, Dynamic response and sliding distance of composite breakwaters under breaking and non-breaking wave attack, Coastal Eng. 58 (2011) 953–969. doi:10.1016/j.coastaleng.2011.03.008.
- [11] T. Zhou, Y. Yin, Z. Ma, J. Chen, G. Zhai, Numerical investigation of breaking waves impact on vertical breakwater with impermeable and porous foundation, Ocean Eng. 280 (2023) 114477. doi:10.1016/j.oceaneng.2023.114477.
- [12] F. Han, W. Wang, X.-W. Zheng, X. Han, W. Shi, X. Li, Investigation of essential parameters for the design of offshore wind turbine based on structural reliability, Reliab. Eng. & System Safety 254 (2025) 110601. doi:10.1016/j.res.2024.110601.
- [13] G. Cuomo, K. ichiro Shimosako, S. Takahashi, Wave-in-deck loads on coastal bridges and the role of air, Coastal Eng. 56 (2009) 793–809. doi:10.1016/j.coastaleng.2009.01.005.
- [14] D. Lucio, J. Lara, A. Tomas, I. Losada, Probabilistic assessment of climate-related impacts and risks in ports, Reliab. Eng. & System Safety 251 (2024) 110333. doi:10.1016/j.res.2024.110333.
- [15] A. Antonini, J. M. W. Brownjohn, D. Dassanayake, A. Raby, J. Bassit, A. Pappas, D. D’Ayala, A Bayesian inverse dynamic approach for impulsive wave loading reconstruction, Coastal Eng. 168 (2021) 103920. doi:10.1016/j.coastaleng.2021.103920.
- [16] M. McCann, B. Ebrahimi, G. Cinar, W. Renteria, A. Stehno, P. Lynett, J. Kaihatu, Field observations of Hurricane Ian’s wave and surge impact in the areas of Fort Myers Beach and Sanibel Island, USA, Coastal Eng. 188 (2024) 104450. doi:10.1016/j.coastaleng.2023.104450.
- [17] J. D. Hansom, A. D. Switzer, J. Pile, Extreme waves: causes, characteristics, and impact on coastal environments and society (Ch.11), in: J. F. Shroder, J. T. Ellis, D. J. Sherman (Eds.), Coastal and Marine Hazards, Risks, and Disasters, Hazards and Disasters Series, Elsevier, Boston, 2015, pp. 307–334. doi:10.1016/B978-0-12-396483-0.00011-X.
- [18] S. M. van Essen, H. C. Seyffert, Designing for dangerous waves – a new ‘Adaptive Screening’ method to predict extreme values of non-linear marine and coastal structure responses to waves, Reliability Eng. & System Safety 264B (2025) 111404. doi:10.1016/j.res.2025.111404.

- [19] H. Bandringa, J. A. Helder, S. M. van Essen, On the validity of CFD for simulating extreme green water loads on ocean-going vessels, in: 39th OMAE Conf., ASME, Virtual, Online, 2020. doi:10.1115/OMAE2020-18290.
- [20] S. M. van Essen, H. C. Seyffert, Finding dangerous waves – Review of methods to obtain wave impact design loads for marine structures (OMAE-22-1110), J. Offshore Mechanics and Arctic Eng. 145 (6) (2023) 060801. doi:10.1115/1.4056888.
- [21] DNV, Recommended Practice RP-C205: Environmental conditions and environmental loads, Det Norske Veritas, Oslo, Norway, 2019.
- [22] DNV, Class Guideline DNV-CG-0130: Wave loads, Det Norske Veritas, Oslo, Norway, 2018.
- [23] DNV, Offshore Technical Guidance DNV-OTG-14: Horizontal wave impact loads for column stabilised units, Det Norske Veritas, Oslo, Norway, 2019.
- [24] BV, Rule Note NR583: Whipping and springing assessment, Bureau Veritas, Paris, France, 2015.
- [25] BV, Rule Note NI638: Guidance for long-term hydro-structure calculations, Bureau Veritas, Paris, France, 2019.
- [26] ABS, Guidance notes on air gap and wave impact analysis for semisubmersibles, American Bureau of Shipping, Spring, USA, 2020.
- [27] ABS, Guide for slamming loads and strength assessment for vessels, American Bureau of Shipping, Spring, USA, 2021.
- [28] ITTC, Recommended Practice 7.5-02-07-02.3: Experiments on rarely occurring events, International Towing Tank Conf., 2017.
- [29] S. M. van Essen, H. C. Seyffert, Designing ships for extreme non-linear responses - the role of the acquisition function in the Adaptive Screening extreme value prediction method, in: 16th PRADS Conf., Ann Arbor, Michigan, USA, 2025. doi:10.5281/zenodo.17305196.
- [30] S. M. van Essen, H. C. Seyffert, Scripts and data underlying the publication that defines and applies the new Adaptive Screening method, for extreme value prediction of non-linear wave-induced responses, 4TU Repository. (2025). doi:10.4121/f1348609-c912-4d06-82b8-197c01f3437b.
- [31] S. M. van Essen, H. C. Seyffert, Scripts and data for PRADS publication that varies the acquisition function of the Adaptive Screening method, 4TU Repository. (2025). doi:10.4121/12777259-c2f6-4b44-b71f-eec5557824d1.
- [32] Y.-B. Xu, L.-L. Liu, Copula-based conditional reliability analysis of slopes in spatially variable soils, Reliability Eng. & System Safety 265 (2026) 111522. doi:10.1016/j.res.2025.111522.
- [33] T. Wang, C. Wang, Y. Zhou, H. Cui, J. Ji, Reliability updating of copula-dependent spatially variable soil slopes based on data-augmented mpr model along slip surfaces, Engineering Geology 356 (2025) 108280. doi:10.1016/j.enggeo.2025.108280.
- [34] X. Qiao, Q. Xie, G. Shi, J. Hu, Seismic reliability assessment for valve hall in converter station based on copula theory, Structures 77 (2025) 109002. doi:https://doi.org/10.1016/j.istruc.2025.109002.
- [35] O. E. Bru-Cordero, C. Castro, V. Leiva, M. C. Jaramillo-Elorza, Confidence intervals for the reliability of dependent systems: integrating frailty models and copula-based methods, Computer Modeling in Eng. and Sciences 143 (2) (2025) 1401–1431. doi:10.32604/cmescs.2025.064487.
- [36] D. Zhang, J. Zhang, M. Yang, S. Bai, F. Wang, Reliability-based design optimization method with correlated variables using adaptive conjugate gradient analysis and copula, Reliability Eng. & System Safety 265 (2026) 111469. doi:10.1016/j.res.2025.111469.
- [37] C. Lu, Y. Feng, C. Fei, D. Teng, Dimensional synchronous modeling-based enhanced kriging algorithm and adaptive copula method for multi-objective synthetical reliability analyses, Chinese Journal of Aeronautics 38 (9) (2025) 103652. doi:10.1016/j.cja.2025.103652.
- [38] P. Mares-Nasarre, M. R. van Gent, O. Morales-Nápoles, A copula-based model to describe the uncertainty of overtopping variables on mound breakwaters, Coastal Eng. 189 (2024) 104483. doi:10.1016/j.coastaleng.2024.104483.
- [39] P. Krupskii, H. Joe, Nonparametric estimation of multivariate tail probabilities and tail dependence coefficients, Journal of Multivariate Analysis 172 (2019) 147–161, dependence Models. doi:10.1016/j.jmva.2019.02.013.
- [40] Gaussian copula-based Bayesian Networks for dynamic loads in mooring systems, Applied Ocean Research 165 (2025) 104809. doi:10.1016/j.apor.2025.104809.
- [41] E. Vanem, E. Fekhari, N. Dimitrov, M. Kelly, A. Cousin, M. Guiton, A joint probability distribution for multivariate wind-wave conditions and discussions on uncertainties (OMAE-23-1131), J. Offshore Mechanics and Arctic Eng. 146 (6) (2024) 061701. doi:10.1115/1.4064498.
- [42] X. Duan, S. Wang, D. Liu, J. Shi, Y. Wu, X. Zhou, A statistical analysis method for significant wave height and spectral peak frequency considering the random and time-varying effects based on copula function and bayesian inference, Ocean Modelling 190 (2024) 102390. doi:10.1016/j.oceomod.2024.102390.
- [43] C. Fang, Y.-L. Xu, Y. Li, J. Li, Serviceability analysis of sea-crossing bridges under correlated wind and wave loads, Reliab. Eng. & System Safety 246 (2024) 110077. doi:10.1016/j.res.2024.110077.
- [44] D. de Waal, P. van Gelder, Modelling of extreme wave heights and periods through copulas, Extremes 8 (2005) 345–356. doi:10.1007/s10687-006-0006-y.
- [45] N. Beck, C. Genest, J. Jalbert, M. Mailhot, Predicting extreme surges from sparse data using a copula-based hierarchical Bayesian spatial model, Environmetrics 31 (2020) e2616. doi:10.1002/env.2616.
- [46] S. Ghosh, B. K. Mallick, A hierarchical Bayesian spatio-temporal model for extreme precipitation events, Environmetrics 22 (2010) 192–204. doi:10.1002/env.1043.
- [47] A. C. Davison, S. A. Padoan, M. Ribatet, Statistical modeling of spatial extremes, Statistical Science 27 (2) (2012) 161–186. doi:10.1214/11-STS376.
- [48] K. Wei, C. Zhou, B. Xu, Spatial distribution models of horizontal and vertical wave impact pressure on the elevated box structure, Applied Ocean Research 125 (2022) 103245. doi:10.1016/j.apor.2022.103245.
- [49] F. Serinaldi, G. Cuomo, Characterizing impulsive wave-in-deck loads on coastal bridges by probabilistic models of impact maxima and rise times, Coastal Engineering 58 (9) (2011) 908–926. doi:10.1016/j.coastaleng.2011.05.010.
- [50] O. Gaidai, G. Storhaug, A. Naess, Extreme large cargo ship panel stresses by bivariate acer method, Ocean Engineering 123 (2016) 432–439. doi:10.1016/j.oceaneng.2016.06.048.
- [51] J. Shen, H. Liu, On the structure dynamic response induced by the dam-break surge impact using multivariate copulas, Ocean Engineering 306 (2024) 118100. doi:10.1016/j.oceaneng.2024.118100.

- [52] G. Cuomo, R. Piscopia, W. Allsop, Evaluation of wave impact loads on caisson breakwaters based on joint probability of impact maxima and rise times, *Coastal Eng.* 58 (1) (2011) 9–27. doi:10.1016/j.coastaleng.2010.08.003.
- [53] Z. Yang, Y. Xu, L. Shi, C. Zhu, Y. Bao, Investigation of methods for the localization and reconstruction of the wave impact on a floating wind turbine pontoon, *J. of Ocean Eng. and Science* (2025). doi:10.1016/j.joes.2025.08.006.
- [54] B. Kramer, A. N. Marques, B. Peherstorfer, U. Villa, K. Willcox, Multifidelity probability estimation via fusion of estimators, *J. Computational Phys.* 392 (2019) 385–402. doi:10.1016/j.jcp.2019.04.071.
- [55] B. Peherstorfer, T. Cui, Y. Marzouk, K. Willcox, Multifidelity importance sampling, *Comput. Methods Appl. Mech. Eng.* 300 (2016) 490–509. doi:10.1016/j.cma.2015.12.002.
- [56] C. Proppe, Reliability estimation with multi-fidelity simulation methods, in: M. Beer, E. Zio (Eds.), 29th ESREL Conf., Research Publishing, Singapore, 2019. doi:10.3850/978-981-11-2724-30168-cd.
- [57] Q. Li, P. Ni, X. Du, Q. Han, Bayesian model updating with variational inference and gaussian copula model, *Comput. Methods Appl. Mech. Eng.* 438 (2025) 117842. doi:10.1016/j.cma.2025.117842.
- [58] P. Ma, Y. Zhang, E. Cai, M. Luo, J. Guo, T. Guo, A copula-based transitional markov chain monte carlo method for bayesian model updating, *Reliability Eng. & System Safety* 265 (2026) 111572. doi:10.1016/j.ress.2025.111572.
- [59] C. Bracken, K. Holman, B. Rajagopalan, H. Moradkhani, A Bayesian hierarchical approach to multivariate nonstationary hydrologic frequency analysis, *Water Resources Research* 54 (2018) 243–255. doi:10.1002/2017WR020403.
- [60] S. M. van Essen, J. Scharnke, H. C. Seyffert, Required test durations for converged short-term wave and impact extreme value statistics - Part 1: ferry dataset, *Marine Struc.* 90 (2023) 103410. doi:10.1016/j.marstruc.2023.103410.
- [61] J. Scharnke, S. M. van Essen, H. C. Seyffert, Required test durations for converged short-term wave and impact extreme value statistics - Part 2: deck box dataset, *Marine Struc.* 90 (2023) 103411. doi:10.1016/j.marstruc.2023.103411.
- [62] R. Torhaug, S. R. Winterstein, A. Braathen, Nonlinear ship loads: stochastic models for extreme response, *J. Ship Research* 42, 1 (1998) 46–55. doi:10.5957/jsr.1998.42.1.46.
- [63] J. S. Dietz, Application of conditional waves as critical wave episodes for extreme loads on marine structures, PhD thesis, Technical University of Denmark, Lyngby, Denmark (2004).
- [64] M. K. Ochi, *Applied Probability and Stochastic Processes in Engineering and Physical Sciences*, John Wiley & Sons, Singapore, 1990.
- [65] H. Bandringa, J. A. Helder, On the validity and sensitivity of CFD simulations for a deterministic breaking wave impact on a semi submersible, in: 37th OMAE Conf., ASME, Madrid, Spain, 2018. doi:10.1115/OMAE2018-78089.
- [66] C. Pákozdi, A. Califano, A. Akselsen, E. Croonenborghs, J. Kim, M. Peric, S. Loubeyre, B. Bouscasse, G. Ducrozet, Xu-Haihua, Joint-industry effort to develop and verify CFD modeling practice for predicting wave impact, in: 41st OMAE Conf., ASME, Hamburg, Germany, 2022. doi:10.1115/OMAE2022-79152.
- [67] S. M. van Essen, C. Monroy, Z. Shen, J. A. Helder, D.-H. Kim, S. Seng, Z. Ge, Screening wave conditions for the occurrence of green water events on sailing ships, *Ocean Eng.* 234 (2021) 109218. doi:10.1016/j.oceaneng.2021.109218.
- [68] S. M. van Essen, H. C. Seyffert, Scripts and data underlying the paper that introduces and validates the Probabilistic Adaptive Screening method, 4TU Repository. (2025). doi:10.4121/be3e7819-dabf-4a21-bb29-5b76179ff696.
- [69] J. N. Sharma, R. G. Dean, Development and evaluation of a procedure for simulating a random directional second order sea surface and associated wave forces, *Ocean Eng. Rep.* 20 (1979).
- [70] S. M. van Essen, T. H. J. Bunnik, J. Scharnke, Statistical uncertainty of ship response to waves as a function of test duration, in: 43rd OMAE Conf., ASME, Singapore, 2024. doi:10.1115/OMAE2024-122486.
- [71] T. H. J. Bunnik, C. T. Stansberg, C. Pákozdi, S. Fouques, L. Somers, Useful indicators for screening of sea states for wave impacts on fixed and floating platforms, in: 37th OMAE Conf., ASME, Madrid, Spain, 2018. doi:10.1115/OMAE2018-78544.
- [72] T. H. J. Bunnik, J. Scharnke, E.-J. de Ridder, Efficient indicators for screening of random waves for wave impacts on a jacket platform and a fixed offshore wind turbine, in: 38th OMAE Conf., ASME, Glasgow, UK, 2019. doi:10.1115/OMAE2019-95481.
- [73] S. M. van Essen, Influence of Wave Variability on Ship Response During Deterministically Repeated Seakeeping Tests at Forward Speed, in: Okada, T., Suzuki, K., Kawamura, Y. (Eds.), 14th PRADS Conf. 2019. Lecture Notes in Civil Engineering, vol 63, Springer, Singapore, Yokohama, Japan, 2021. doi:10.1007/978-981-15-4624-2_54.
- [74] O. Gramstad, T. B. Johannessen, G. Lian, Long-term analysis of wave-induced loads using High Order Spectral Method and direct sampling of extreme wave events, *Marine Struc.* 103473 (2023). doi:10.1016/j.marstruc.2023.103473.
- [75] T. H. J. Bunnik, J. A. Helder, E.-J. de Ridder, Deterministic simulation of breaking wave impact and flexible response of a fixed offshore wind turbine, in: 34th OMAE Conf., ASME, St. John's, Newfoundland, Canada, 2015. doi:10.1115/OMAE2015-41989.
- [76] S. Guth, E. Katsidoniotaki, T. P. Sapsis, Statistical modeling of fully nonlinear hydrodynamic loads on offshore wind turbine monopile foundations using wave episodes and targeted CFD simulations through active sampling, *Wind Energy* 28 (2023) 1–26. doi:10.1002/we.2880.
- [77] T. B. Johannessen, Ø. Lande, Long term analysis of steep and breaking wave properties by event matching, in: 37th OMAE Conf., ASME, Madrid, Spain, 2018. doi:10.1115/OMAE2018-78283.
- [78] S. R. Winterstein, T. C. Ude, C. A. Cornell, P. Bjerager, S. Haver, Environmental parameters for extreme response: inverse FORM with omission factors, in: Int. Conf. Struct. Saf. Reliab., Innsbruck, Austria, 1993.
- [79] A. B. Huseby, E. Vanem, B. Natvig, A new approach to environmental contours for ocean engineering applications based on direct Monte Carlo simulations, *Ocean Eng.* 60 (2013) 124–135. doi:10.1016/j.oceaneng.2012.12.034.
- [80] E. B. L. Mackay, C. Murphy-Barltrop, P. Jonathan, The SPAR model: a new paradigm for multivariate extremes: application to joint distributions of metocean variables (omae-24-1018), *J. Offshore Mechanics and Arctic Eng.* 147 (2025) 011205:1–10. doi:10.1115/1.4065968.
- [81] M. Speers, D. Randell, J. Tawn, P. Jonathan, Estimating metocean environments associated with extreme structural response to demonstrate the dangers of environmental contour methods, *Ocean Eng.* 311 (2024) 118754. doi:10.1016/j.oceaneng.2024.118754.

- [82] A. F. Haselsteiner, R. G. Coe, L. Manuel, W. Chai, B. Leira, G. Clarindo, C. Guedes Soares, Ásta Hannesdóttir, N. Dimitrov, A. Sander, J.-H. Ohlendorf, K.-D. Thoben, G. de Hauteclocque, E. Mackay, P. Jonathan, C. Qiao, A. Myers, A. Rode, A. Hildebrandt, B. Schmidt, E. Vanem, A. B. Huseby, A benchmarking exercise for environmental contours, *Ocean Eng.* 236 (2021) 109504. doi:10.1016/j.oceaneng.2021.109504.
- [83] G. de Hauteclocque, E. Mackay, E. Vanem, Quantitative comparison of environmental contour approaches, *Ocean Eng.* 245 (2022) 110374. doi:10.1016/j.oceaneng.2021.110374.
- [84] O. Gramstad, C. Agrell, E. Bitner-Gregersen, B. Guo, E. Ruth, E. Vanem, Sequential sampling method using Gaussian process regression for estimating extreme structural response, *Mar. Struct.* 72 (2020). doi:10.1016/j.marstruc.2020.102780.
- [85] H. Wang, O. Gramstad, S. Schär, S. Marelli, E. Vanem, Comparison of probabilistic structural reliability methods for ultimate limit state assessment of wind turbines, *Structural Safety* 111 (2024) 102502. doi:10.1016/j.strusafe.2024.102502.
- [86] A. Sklar, Fonctions de répartition à n dimensions et leurs marges, in: *Publications de l'Institut de statistique de l'Université de Paris*, Vol. 8, 1959, pp. 229–231.
- [87] F. Salmon, Recipe for disaster – the formula that killed Wall Street, *Wired Magazine* 17.03, February 2009 (2009). URL <https://www.wired.com/2009/02/wp-quant/>